

1978

A toroidal fusion reactor design based on the reversed-field pinch

Randy Lee Hagenson
Iowa State University

Follow this and additional works at: <https://lib.dr.iastate.edu/rtd>

 Part of the [Nuclear Engineering Commons](#), and the [Oil, Gas, and Energy Commons](#)

Recommended Citation

Hagenson, Randy Lee, "A toroidal fusion reactor design based on the reversed-field pinch " (1978). *Retrospective Theses and Dissertations*. 6455.
<https://lib.dr.iastate.edu/rtd/6455>

This Dissertation is brought to you for free and open access by the Iowa State University Capstones, Theses and Dissertations at Iowa State University Digital Repository. It has been accepted for inclusion in Retrospective Theses and Dissertations by an authorized administrator of Iowa State University Digital Repository. For more information, please contact digirep@iastate.edu.

INFORMATION TO USERS

This material was produced from a microfilm copy of the original document. While the most advanced technological means to photograph and reproduce this document have been used, the quality is heavily dependent upon the quality of the original submitted.

The following explanation of techniques is provided to help you understand markings or patterns which may appear on this reproduction.

1. The sign or "target" for pages apparently lacking from the document photographed is "Missing Page(s)". If it was possible to obtain the missing page(s) or section, they are spliced into the film along with adjacent pages. This may have necessitated cutting thru an image and duplicating adjacent pages to insure you complete continuity.
2. When an image on the film is obliterated with a large round black mark, it is an indication that the photographer suspected that the copy may have moved during exposure and thus cause a blurred image. You will find a good image of the page in the adjacent frame.
3. When a map, drawing or chart, etc., was part of the material being photographed the photographer followed a definite method in "sectioning" the material. It is customary to begin photoing at the upper left hand corner of a large sheet and to continue photoing from left to right in equal sections with a small overlap. If necessary, sectioning is continued again — beginning below the first row and continuing on until complete.
4. The majority of users indicate that the textual content is of greatest value, however, a somewhat higher quality reproduction could be made from "photographs" if essential to the understanding of the dissertation. Silver prints of "photographs" may be ordered at additional charge by writing the Order Department, giving the catalog number, title, author and specific pages you wish reproduced.
5. PLEASE NOTE: Some pages may have indistinct print. Filmed as received.

University Microfilms International

300 North Zeeb Road
Ann Arbor, Michigan 48106 USA
St. John's Road, Tyler's Green
High Wycombe, Bucks, England HP10 8HR

7813228

HAGENSON, RANDY LEE
A TOROIDAL FUSION REACTOR DESIGN BASED ON THE
REVERSED-FIELD PINCH.

IOWA STATE UNIVERSITY, PH.D., 1978

University
Microfilms
International 300 N ZEEB ROAD, ANN ARBOR, MI 48106

A toroidal fusion reactor design based
on the reversed-field pinch

by

Randy Lee Hagenson

A Dissertation Submitted to the
Graduate Faculty in Partial Fulfillment of
The Requirements for the Degree of
DOCTOR OF PHILOSOPHY

Department: Chemical Engineering and Nuclear Engineering

Major: Nuclear Engineering

Approved:

Signature was redacted for privacy.

In Charge of Major Work

Signature was redacted for privacy.

For the Major Department

Signature was redacted for privacy.

For the Graduate College

Iowa State University
Ames, Iowa

1978

TABLE OF CONTENTS

	Page
ABSTRACT	vii
I. INTRODUCTION	1
A. Summary of the Reversed-Field Pinch Concept	1
B. Reactor Considerations	5
C. Objectives	9
II. LITERATURE REVIEW	10
A. Theory	10
B. Experiments	17
C. Reactor Studies	21
III. DESCRIPTION OF ENERGY BALANCE	24
A. General Model	24
B. Plasma and Magnetic Field Models	26
C. Plasma Energy Balance	30
D. Magnetic Energy Storage and Joule Losses	34
E. Computational Procedure	37
IV. RESULTS	39
A. Reactor Startup Phase	39
B. Thermonuclear Burn Cycles	41
C. Plasma Quench	49
D. Operating Point(s) Determination	51

	Page
V. FINAL SYSTEM DESIGN	61
A. General Reactor Description	61
B. Consideration of Major System Components	67
VI. SUMMARY AND CONCLUSIONS	83
VII. TOPICS FOR FURTHER STUDY	87
VIII. LITERATURE CITED	88
IX. ACKNOWLEDGMENTS	95
X. APPENDIX	96

LIST OF TABLES

	Page
Table 1. Summary of reversed-field pinch parameters	18
Table 2. Dimensions used in RFPR energy-balance study	44
Table 3. Summary of typical RFPR parameters	57
Table 4. Homopolar specifications	82

LIST OF FIGURES

	Page
Fig. 1. In the toroidal system R is taken as the major radius and r_w as the minor radius. The minor axis of the torus is denoted by z , and the angle about z is given by θ .	2
Fig. 2. Field profiles of various fusion concepts.	3
Fig. 3. Cross-sectional drawing of the envisioned RFPR.	8
Fig. 4. Sample MHD stable pressure and field profiles for a linear pinch showing the effect of increasing the pressure on the location of the conducting wall for stability (13).	13
Fig. 5. Complete RFPR energy balance used in conjunction with a time-dependent RFP plasma model to evaluate a range of reactor operating points. Refer to text for notation.	25
Fig. 6. Comparison of assumed poloidal B_θ and toroidal B_z fields and actual MHD stable field profiles (13).	28
Fig. 7. Generalized pressure-volume diagram for the RFPR. Magnetic field pressures, plasma pressure p , and the plasma direct-conversion work W_{DC} for high-beta plasma expansion against a magnetic field are shown for the assumed sharp-boundary plasma model.	42
Fig. 8. Lines of constant Q_E for various first-wall radii r_w and maximum average toroidal current densities j_z (solid curves) where a 50%-50% D-T fuel mixture is used. The dotted-dashed curves are lines of constant first-wall ((0.3 mm)Al ₂ O ₃ /(2 mm)Nb-1Zr) surface temperature rise $\Delta T_w(k)$.	46
Fig. 9. Dependence of the engineering Q-value Q_E on the initial plasma tritium fraction f_T for 90% burnup of the available tritium in the plasma.	48
Fig. 10. Lines of constant Q_E for various first-wall radii r_w and maximum average toroidal current densities j_z (solid curves) where a 90%-10% D-T fuel mixture is used. The dotted-dashed curves are lines of constant first-wall ((0.3 mm)Al ₂ O ₃ /(5 mm)Nb-1Zr) surface temperature rise $\Delta T_w(k)$.	50

	Page
Fig. 11. Time-dependence of plasma and energy quantities for the 50%-50% D-T operating point summarized in Table 3.	53
Fig. 12. Time-dependence of plasma and energy quantities for the 90%-10% D-T operating point summarized in Table 3.	54
Fig. 13. Dependence of Q_E on the magnetic energy transfer/storage efficiency η_{ETS} for both cases investigated.	55
Fig. 14. Time-dependence of various plasma parameters and dominant powers for a tokamak-like RFPR startup.	56
Fig. 15. Plan and elevation view of 750 MWe (net) RFPR.	62
Fig. 16. Schematic diagram of the primary-coolant circuit illustrating the major lithium flow paths.	63
Fig. 17. Isometric view of 2-m-long RFPR reactor modules (vacuum vessel, blanket, toroidal field coil) and associated poloidal field coil assembly and iron-core pieces.	65
Fig. 18. Time dependence of the blanket temperature distribution for the 50%-50% D-T burn cycle summarized in Table 3.	69
Fig. 19. Time dependence of lithium coolant flow in the RFPR blanket for the 50%-50% D-T fuel mixture case.	71
Fig. 20. Dependence of first-wall temperature and stress during the ignition, burn, quench, and plasma cooling periods associated with the 50%-50% D-T burn cycle given in Table 3.	73
Fig. 21. Dependence of first-wall temperature and stress during the ignition, burn, quench, and plasma cooling periods associated with the 90%-10% D-T burn cycle given in Table 3.	74
Fig. 22. Schematic diagram of homopolar-generator driven circuit for both TFC and PFC systems. The voltage $V \sim 4-5$ kV, the rise time $\tau_R \sim 100$ ms, and $\tau_B \sim 1-6$ s.	76

ABSTRACT

The toroidal reversed-field pinch (RFP) achieves gross equilibrium and stability with a combination of high shear and wall stabilization, rather than the imposition of tokamak-like q -constraints. Consequently, confinement is provided primarily by poloidal magnetic fields, poloidal betas as large as ~ 0.58 are obtainable, the high ohmic-heating (toroidal) current densities promise a sole means of heating a D-T plasma to ignition, and the plasma aspect ratio is not limited by stability/equilibrium constraints. A reactor-like plasma model has been developed in order to quantify and to assess the general features of a power system based upon RFP confinement. An "operating point" has been generated on the basis of this plasma model and a relatively detailed engineering energy balance. These results are used to generate a conceptual engineering model of the reversed-field pinch reactor (RFPR) which includes a general description of a 750 MWe power plant and the preliminary consideration of vacuum/fueling, first wall, blanket, magnet coils, iron core, and the energy storage/transfer system.

I. INTRODUCTION

A. Summary of the Reversed-Field Pinch Concept

The desire for power production from fusion reactions has led to the pursuit of many plasma confinement schemes. The present experimental goal of containing a reacting plasma for a sufficient time to achieve a net energy output has been difficult to attain. Even when plasma physics problems are overcome, the economics of the reactor system may be unfavorable and render a particular concept useless. The purpose of this thesis is to determine the potential of a fusion reactor system based on reversed-field pinch confinement. Theoretical predictions (Sec. II.A) and experimental observation (Sec. II.B) provide the basis for the present optimism that stable plasma confinement may be achievable for time periods sufficient to make an economic reactor system.

Toroidal pinch systems confine the plasma using an azimuthal field B_θ produced by a toroidal current flowing through the plasma and a toroidal field B_z applied from external coils where the coordinate notation is shown in Fig. 1. Two basic approaches have emerged that seek to obtain stable configurations. The first achieves magnetohydrodynamic (MHD) stability by operating below the Kruskal-Shafranov current limit (1,2) which implies that unstable modes would require magnetic field wavelengths longer than the major circumference of the torus. This translates into $q > 1$ where

$$q = (B_z/B_\theta)/A \quad . \quad (1.1)$$

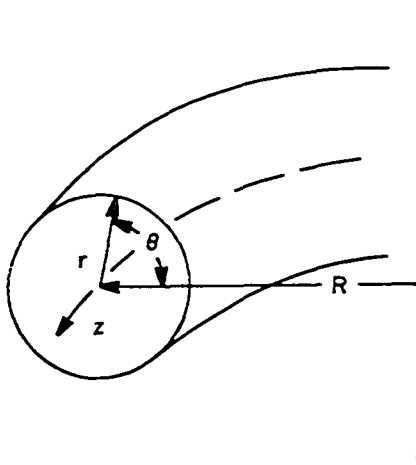


Fig. 1. In the toroidal system R is taken as the major radius and r_w as the minor radius. The minor axis of the torus is denoted by z , and the angle about z is given by θ .

The aspect ratio A is R/r_w where r_w is the first-wall radius. The major device utilizing this concept is the tokamak (3-6) whose field profiles are also shown in Fig. 2. Maintaining $q > 1$ requires small values of B_θ/B_z which leads to low values of total β (plasma pressure/total magnetic pressure). It is desirable, however, to have a high total β because the power density is proportional to the square of the number density and $n \propto \beta B^2$, so for a constant magnetic field the power output is directly related to β^2 . Present tokamak designs for increasing the total plasma beta are based upon the noncircular plasma concept (5,6) and the flux conserving tokamak (6). These techniques are envisioned to allow $\beta = 3-10\%$ and still maintain MHD stability. Belt pinches (7,8) shown in Fig. 2 and high-beta tokamaks (8,9) also seek to increase β values. The screw pinch (8-10) shown in Fig. 2 is theoretically stable for $q \sim 0.7-1.5$ with total β up to 25%. The stabilizing influence of

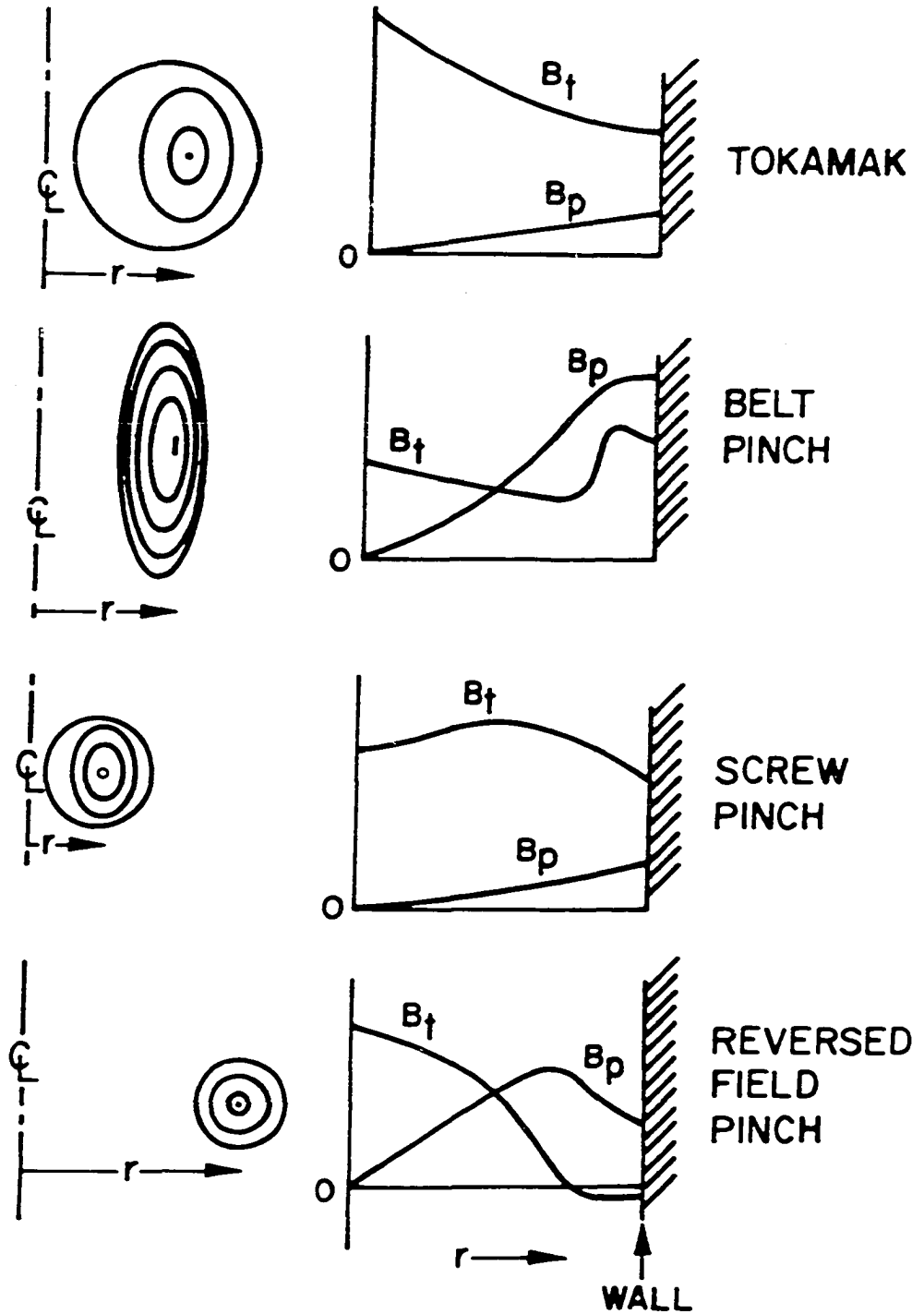


Fig. 2. Field profiles of various fusion concepts.

pressureless plasma currents outside the plasma column achieve these high values of β .

As seen from Eq. (1.1), small aspect ratios are also desirable for $q > 1$. This implies "tight" tori leading to inhomogeneous toroidal B_z fields which produces many trapped particle instabilities and enhances the particle and energy diffusion rates (3,4).

In the second major approach a conducting shell (or external conductors) eliminates grossly unstable modes with magnetic field wavelengths that are now greater than the minor radius of the device. Localized modes are avoided by using a strongly sheared magnetic field. The reversed-field pinch (RFP) utilizes this approach (11-13) and is shown in Fig. 2. The Kruskal-Shafranov limit (1,2) no longer applies and large ohmic heating currents are possible. The restrictions of small aspect ratios and small values of B_θ/B_z are therefore, removed. Theoretical values of total β equal to $\sim 40\%$ are predicted.

Numerous methods (11-13) of producing the desired RFP profiles have been considered. Simply inducing a plasma current in the presence of an initial bias field B_{z0} produces a discharge which is initially unstable. Wall contact and unstable MHD modes allow the plasma to spontaneously produce a reversed toroidal field in the outermost region of the discharge. This phenomena of self-field reversal relaxes the plasma into a quiescent mode of operation.

The RFP may also be generated by programming the currents in the toroidal field windings. The reversed field is thereby imposed on the plasma, and the desired profiles can be produced without the initial turbulent phase that characterizes the self-reversal mode. Many of the

present experiments (Sec. II.B) use this approach, however, the field risetimes must be comparable to the growth rates (\sim sound speed in the plasma) of the unstable plasma modes. These times are too short for reactor systems in which rotating machinery is used to store the magnetic field energy between pulses. Aiding the self-reversal process with field programming is considered feasible for relatively slow rise-time systems. The device is often started as a tokamak discharge with an initial toroidal B_{z0} field and $q > 1$. As the plasma current is increased, the toroidal field outside the plasma column is reversed and the plasma likely passes through many unstable states as q falls below one until a stable RFP field profile is established. Other methods of field programming such as increasing the toroidal bias field as the current is increased to give $q < 1$ during startup are also postulated. A combination of self-reversal and field programming will hopefully minimize the wall interaction during the plasma initiation and burn.

B. Reactor Considerations

The reversed-field pinch reactor (RFPR) offers many advantages when compared to q -stabilized systems. The RFPR would operate well above the Kruskal-Shafranov current limit (1,2) and may, therefore, achieve ignition utilizing the high ohmic heating rates. The main confining field, B_{θ} , varies as $1/r$ outside the plasma, reducing magnetic energy storage requirements and magnet stresses when compared to devices which have uniform toroidal fields outside the plasma. The unrestricted

aspect ratio should lead to more open systems and reduced construction and maintenance problems.

The operating scheme investigated here for a RFPR is that of a pulsed, high- β system, in which the burn time is a fraction of the energy confinement time. This "batch" burn process implies that no refueling is needed during the burn. The problem of wall interaction with a diffuse plasma edge is minimized by the short burn periods, and divertors are not required. The vigorous plasma burn is not easily degraded by the influx of impurities.

Pulsed systems allow the use of room-temperature coils because the output power (proportional to β^2 for a constant confining field) can be made much larger than joule losses in a high- β system. The need for large superconducting coils outside of thick blankets and blanket shields is obviated, which represents considerable cost reductions. The energy balance is enhanced by alpha-particle reaction products expanding against the magnetic field and forcing flux out of the magnet coils. This direct-conversion of $\sim 60\%$ of the alpha-particle energy to electrical energy through the magnet coils occurs with $\sim 100\%$ efficiency.

Varying the burn pulse in frequency and amplitude allows control of the output power. Thermal fluctuations in the primary coolant loop and blanket structure are small because "off" times less than 10 s are short compared to the thermal time constants. Liquid lithium can be utilized for breeding tritium and providing cooling with little pumping energy loss. In steady-state systems the lithium must be pumped across strong magnetic fields, whereas pulsed systems may be operated with small lithium flows during the burn when fields are present.

Operation in a pulsed mode also presents inherent disadvantages when compared to quasi-steady-state systems. Cyclic thermal/mechanical loading of the first-wall and blanket imposes operational constraints. Thermal fatigue of the first wall is a particularly crucial problem. The magnetic energy must be switched into the reactor each burn cycle, and recovered by the energy storage device with high efficiency to achieve an acceptable energy balance. Efficient energy transfer requires reliable switching and pulsed energy power supplies such as homopolar generators. This pulsed mode of operation implies that the highly energetic plasma must be nondestructively contained and quenched without excessive magnetic field dissipation. Feedback control of the plasma may be required at high- β to achieve the required stable configurations.

A schematic drawing of the envisioned RFPR in Fig. 3 shows the location of the major system components. A reference first-wall system (14) of Al_2O_3 bonded to Nb-1%Zr structural alloy is used for first-wall heat transfer calculations. The alumina provides protection against high-z impurities due to sputtering. The blanket utilizes a lead multiplying region followed by ^6Li , resulting in tritium breeding ratios of 1.10 for a 0.35-m thick blanket (15). A conventional steam cycle converts the thermal blanket energy into electrical energy with an assumed 40% efficiency. The room temperature poloidal and toroidal field coils are outside of the lithium cooled blanket. An iron core couples the poloidal coil current from the homopolar energy store (16) to the plasma with nearly unity coupling, accomplished by not saturating the iron core.

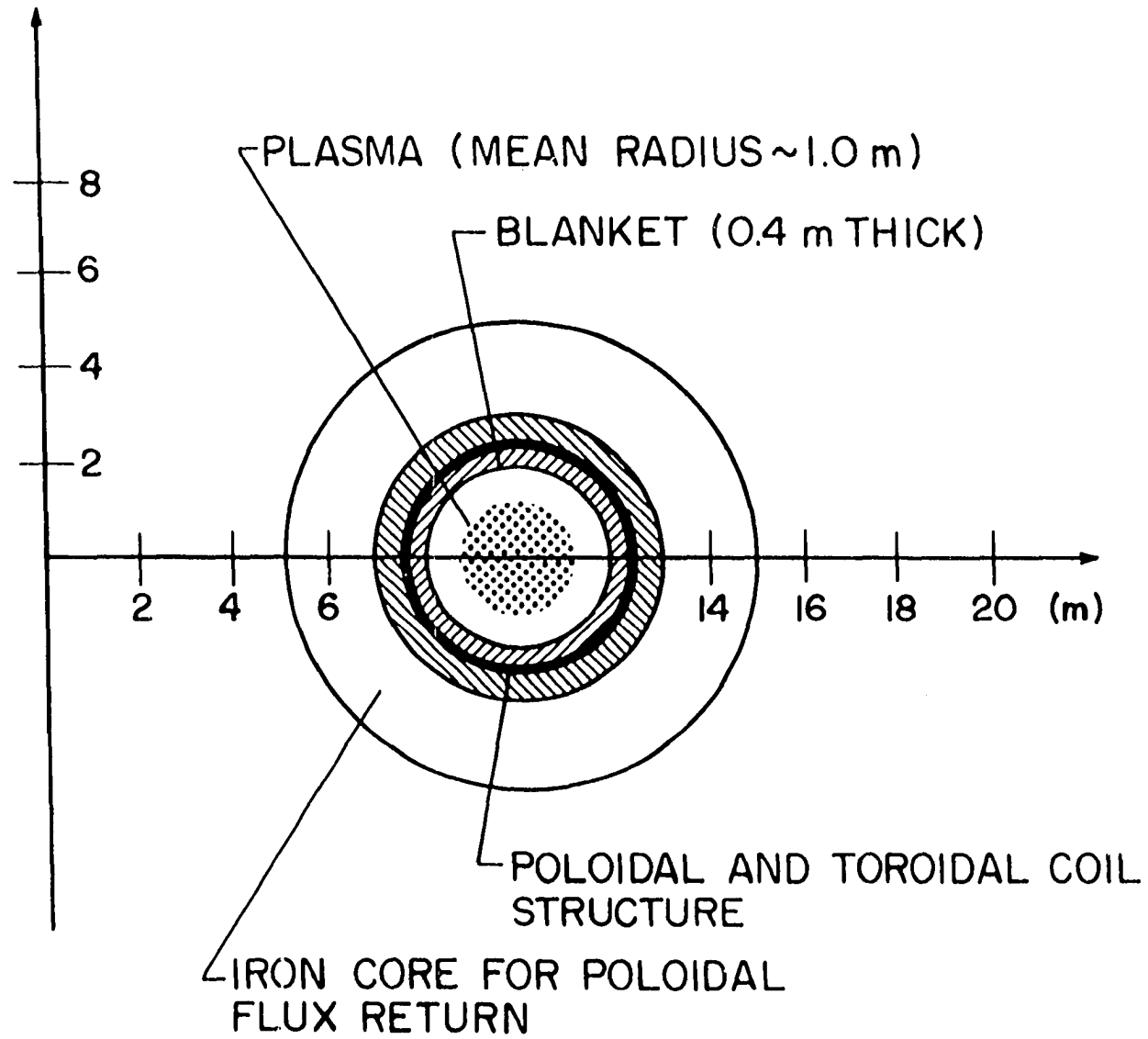


Fig. 3. Cross-sectional drawing of the envisioned RFPR.

C. Objectives

This thesis investigates possible operating schemes for a RFPR. A realistic energy balance defines the important energy flows throughout the system. The reactor performance is then evaluated for various first-wall radii, plasma current densities, plasma number densities, and deuterium-tritium DT fractions. A zero-dimension plasma engineering code is developed to calculate the burn dynamics for a plasma confined by ideal poloidal and toroidal fields modeled by Bessel functions. Alpha-particle thermalization using Fokker-Planck formulism, classical particle diffusion and thermal conduction, ohmic heating, and radiation losses are included.

Potential operating points for the RFPR are presented which include startup and pre-quench phases. The final system design includes a general reactor description, including preliminary considerations of the required energy storage systems with associated circuits, magnet coils, lithium blanket, and the first wall. The results of the analyses presented herein are used to identify a physics operating point for the RFPR rather than to generate a detailed engineering design for the system.

II. LITERATURE REVIEW

A. Theory

The pinch discharge is one of the earliest fusion concepts to be proposed. The simple pinch is a resistively heated current-carrying conductor being radially compressed by the azimuthal field generated by the current. The theory of a constricted gas current was initially developed in 1934 and is presented in Glasstone and Lovberg (17). The simple pinch is, however, very unstable to both sausage and kink-type instabilities. A local constriction of the plasma column enhances the field pressure ($\propto 1/r^2$) at that point causing further contraction and complete current disruption as the sausage mode progresses. The plasma may also remain circular in cross section and develop a kink. The lines of force due to the current in the plasma are brought closer together on the inside of the kink and farther apart on the outside. Once a slight kink develops, the mode grows until the plasma strikes the walls. Theories were then developed that quantitatively explained the behavior of instabilities and predicted the fields necessary to produce a stable pinch.

Early theoretical work on pinch discharges utilized normal mode analysis (17-24) which describes small-amplitude perturbations of the plasma in terms of Fourier components. Small amplitude displacements ξ are represented by

$$\xi = \xi(r) \exp [i(m\theta + kz + \gamma t)] \quad (2.1)$$

where m is the azimuthal periodicity of a particular deformation mode, k is the longitudinal wave number, and γ determines the growth rate of the

perturbation. If γ^2 is positive, the perturbation is periodic in time and stable. For γ^2 negative, the disturbance grows exponentially in time and the system is unstable.

In 1954 Kruskal and Schwarzschild (19) applied the above analysis to a cylindrical sharp-boundary plasma carrying a toroidal current, I_z , in an infinitely thin surface layer. Using no bias field B_z , it was found that the system was unstable for $m = 0$ (sausage instability) and 1 (kink instability). Tayler (20) showed in 1957 that all mode numbers m were unstable in this simple pinch, and the growth rates $1/\gamma$ were of the same magnitude as the sound speed in the plasma.

The sharp boundary model was then extended (1956-1958) to include an axial field B_z both inside and outside of the plasma, and a conducting shell encircling the pinch (21-24). The $m = 0$ and $m = 2$ modes were stabilized using only an axial field, whereas a conducting shell was needed to stabilize the $m = 1$ mode. The sharp boundary stability criteria is given approximately by

$$x > \frac{1}{5(1-\beta_\theta)} , \quad \beta_\theta < 0.5, \quad (2.2)$$

where β_θ is the plasma pressure inside the pinch divided by the poloidal field pressure at the surface of the pinch, and x is the plasma radius r_p divided by the first-wall radius r_w .

Sharp boundary pinches were not encountered experimentally, and a model which allowed current to permeate the plasma region was needed. A necessary, although not sufficient, condition for a diffuse linear pinch given in 1958 is the Suydam criteria (25)

$$\frac{r}{4} \left(\frac{1}{v} \frac{dv}{dr} \right)^2 + \frac{2\mu_0}{B_z^2} \frac{dp}{dr} > 0, \quad (2.3)$$

where

$$v = \frac{B_\theta}{rB_z} \quad (2.4)$$

represents the number of rotations of a field line per unit length along the z-coordinate. The localized plasma pressure is p and $\mu_0 = 4\pi \times 10^{-7}$ h/m. The quantity $(1/v)(dv/dr)$ is the rate of change in pitch angle with radial distance and is called the "shear" of the field. As seen in Eq. (2.3) high shear is desirable for stability. Sample stable pressure and field profiles which satisfy this criteria are shown in Fig. 4. As $r \rightarrow 0$ the shear of the fields vanishes, and Eq. (2.3) is satisfied by a positive pressure gradient dp/dr . Clearly the pressure gradient must be negative near the outer edge of the discharge as the pressure is reduced to near zero at the wall. This destabilizing effect is cancelled by highly sheared fields in the outer regions resulting from the reversed toroidal field.

Using ideal MHD theory, necessary and sufficient conditions were found by Newcomb (26) in 1960 for a linear diffuse pinch. Stability occurs for all m and k values if and only if the pinch is stable for $m = 0, k \rightarrow 0$ and $m = 1, -\infty < k < \infty$. The application of this criteria involves the solution of the Euler-Lagrange equation (18). This formulism finds the displacement $\xi(r)$ which minimizes the systems' potential energy. The stability criteria predicts that any displacement from the equilibrium configuration yields an increase in potential

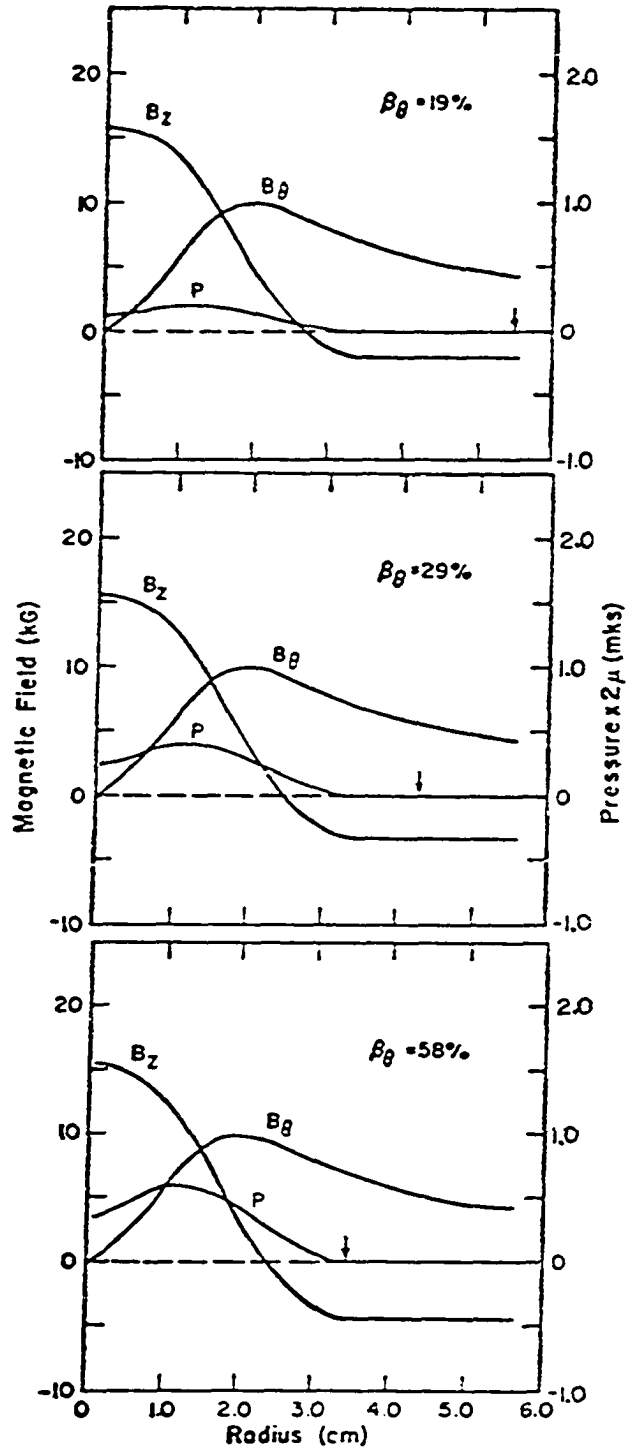


Fig. 4. Sample MHD stable pressure and field profiles for a linear pinch showing the effect of increasing the pressure on the location of the conducting wall for stability (13).

energy, i.e., requires work to be done on the system. This calculation and other methods used in 1960 by Furth and Suydam (27,28) of investigating stability generally require numerical computer solutions. Recent (1971-1974) calculations (29-31) yield stable reversed-field profiles as shown in Fig. 4. The important conditions for stability are positive total axial flux, $\beta_0 \leq (0.5 + \text{local } \beta \text{ value, where } B_z = 0)$ and the profile must satisfy Suydam's criteria. The first two conditions are important for reactor considerations and are monitored in this study by the zero-dimensional models. The last condition would require a one-dimensional MHD code, however, so the precise shape of a stable plasma profile is not included when a reactor energy balance is being considered.

Robinson (31) noted in 1971 that a stable configuration also requires that no minimum in the pitch $l/v = rB_z/B_0$ versus radius be present (31). The pitch l/v must fall monotonically from $r = 0$ to the conducting wall. In the vacuum region, $B_z = \text{constant}$, $B_0 \propto 1/r$ and the resultant pitch varies as r^2 . If both B_z and B_0 are positive, the pitch is increasing in the vacuum region and a pitch minimum will occur. Reversing the B_z field in the vacuum region allows the pitch to continue to fall outside the plasma. A current-free vacuum region is then allowed in a RFP between the plasma and the wall.

The calculation of MHD stable equilibria has been extended to toroidal coordinates (32-34) in 1972 using numerical techniques, where the stability of localized modes is determined by the Mercier (32) criterion (toroidal analog of the Suydam criterion) published in 1960. The RFP toroidal configuration produces enhanced stability margins for

aspect ratios (major radius/minor radius) of 1-5, when compared to a linear device. For aspect ratios approaching 1.0, however, extreme toroidal effects induce instabilities. Stable equilibria exist when $\beta_0 \lesssim 0.6$ for aspect ratios greater than ~ 2 . Aspect ratios greater than ~ 5 allow the use of linear pinch stability theory with substantially the same results.

The stability criteria predicted by ideal MHD theory is used for the physics constraints in the reactor calculations. A large body of additional information has been added to the theory of pinches since 1970. Nonideal MHD theory has been used to investigate resistive instabilities using a time-dependent code that solves the linearized equations of motion (35,36). Including compressibility, finite resistivity, viscosity, and thermal conductivity, unstable resistive tearing modes are possible for ideal MHD stable profiles. Theoretically stable resistive configurations have been found (37) for total $\beta \sim 30\%$. A Vlasov-fluid model (38) has also been used to study RFP configurations. This model predicts better stability margins than does ideal MHD theory. Microinstability theory is also being actively pursued and is summarized in Reference 12.

The behavior of a RFP during startup and operation has been investigated analytically and numerically. The self-reversal of the outer toroidal field, observed in RFP experiments (Sec. II.B), has been predicted theoretically (39,40). For a slight energy dissipation, the pinch will naturally relax to a state of minimum energy. For $\theta > 1.2$ ($\theta = B_\theta(\text{wall})/\langle B_z \rangle$, $\langle B_z \rangle = 2r_w^{-2} \int_0^r B_z r dr$) the lowest energy state

inside a perfectly conducting wall has a force-free region with a reversed field. For very fast field programmed systems, a global energy and pressure balance has produced the following theorem (41): If the plasma current risetime is much faster than the flux diffusion time, static equilibrium cannot be achieved after the poloidal field has diffused to a uniform current distribution unless losses or plasma pressure at the wall are present. This situation implies that the localized plasma pressure may become too high during a very fast start-up, and a turbulent phase may result.

Numerical modeling of the experimental plasma behavior in ZT-I (Sec. II.B) has also been performed. A time-dependent, one-dimension MHD code (34) with anisotropic electrical resistivity, heat conduction, and impurity radiation has been used to investigate the postimplosion phase of ZT-I. The electrical resistivity appears to be nearly classical on axis and must increase by two orders of magnitude from the axis to the discharge tube wall in order to approximate the experimental results. If this increase is interpreted to be classical (resistivity $\eta \propto T^{-3/2}$) then the temperature must fall from ~ 20 eV on axis to a few eV at the wall. More precise temperature measurements are needed to answer the question of anomalous versus classical resistivity. The energy loss to the wall can be taken into account by enhanced transport or by impurity radiation, assuming 1% oxygen and 1% carbon. For the same problem, a hybrid code (42) that treats ions as particles and electrons as a fluid has been used to model the discharge. The field diffusion during the pinch phases has been matched well using an enhanced resistivity. These

simulations are carried out for the 5-15 μ s containment times of the experimental discharge.

B. Experiments

A large number (17,18,43) of linear pinch devices were constructed during the years 1957-1958 in which the electrodes were inserted directly into the plasma at the ends of the tube. Current rise rates of 10^{10} to 10^{11} A/s and initial gas pressures of 2 to 10^3 mTorr were readily obtainable in devices with lengths from a few inches to several feet and diameters up to two feet. Measurements performed away from the ends appeared not to be dominated by end effects such as impurities and electrode cooling due to the short confinement times. These experiments were in general agreement that the expected instabilities discussed in Sec. II.A. propagated with the sound speed in the plasma. Many of these experiments (17,18,43) also included a bias field which suppressed the $m = 0$ mode. According to sharp-boundary theory (Sec. II.A), using a bias field and a conducting shell around the plasma may provide a stable plasma configuration. This theory was insufficient to predict the behavior of a diffuse plasma and the $m = 1$ mode persisted. Using Suydam's criteria for a diffuse-current layer, the possibility of improved stability by imposing a reversed field B_z outside the plasma column, or utilizing self-reversal during the current initiation, led to the toroidal RFP experiments listed in Table 1.

One of the first experiments to impose a reversed field, by Ohkawa et al. (44) in 1963, is designated as RFP1 in Table 1. By using an

initial bias field $B_{z0} \sim 0.1$ T and programming the magnetic and electric fields to reverse outside of the pinch during the current rise, the plasma lasted for 10 to 15 μ s at ion temperatures up to 130 eV. Plasma compression increased the density by a factor of ~ 5 which resulted in peak ion densities of $3 \times 10^{22} \text{ m}^{-3}$. Without programming, MHD instabilities forced the plasma to the wall within 3 μ s.

Table 1. Summary of reversed-field pinch parameters^a

Experiment Designation	Composition of First Wall	First-Wall Radius r_w (cm)	Major Radius R (cm)	Plasma Current I_z (kA)	Filling Pressure P_A (mTorr)
RFPI	Alumina	3.5	25	20	90-100
ZETA	Stainless Steel	50	150	100-900	0.25-2.0
HBTX	Quartz	6.5	100	40-110	40
ETA-BETA	Quartz	5	40	30-150	20-80
ETL-TPE-1	Pyrex	5	40	80-120	30-50
STP	Quartz	4	12	50	20-30
ZT-I	Alumina	5	37	30-200	10-100
ZT-S	Alumina	7.7	40	30-140	10-100

^aExperiments described in text.

The relatively slow current risetime (~ 1 ms) for the ZETA device (45-49), initially operated in 1958, induced voltages of only ~ 100 V/m

and allowed the use of a metallic first wall. Sustaining plasma currents for 1-3 ms through a low pressure gas in the presence of a stabilizing field B_{z0} (0.02 - 0.1 T) produced plasma temperatures of 10-50 eV and energy confinement times of $\tau_E \sim 100 \mu s$. Values of $\Theta_0 = 2-5$ ($\Theta_0 = B_\theta(\text{wall})/B_{z0}$) were achieved with β_θ up to 10%. A reversed field was not imposed on the outside of the plasma. Continuing experimental studies (47) made from 1965-1968 exhibited a period of improved stability for times up to 3 ms at electron temperatures of 100-200 eV. The quiescence occurred only when both the magnetic and electric fields were reversed in the outer regions of the plasma with $\Theta_0 > 1.8$. Recent analysis of old ZETA experimental data (48) has produced substantially the same conclusions where energy containment times were estimated to be 3-10 ms during the quiescent state at $\beta_\theta \sim 10\%$. In this experiment no reverse field was imposed on the plasma; self-reversal occurred when the plasma relaxed to a state of minimum potential energy.

In HBTX (50,51), reversed-field configurations were produced by fast programming. Using $\Theta \sim 2$ suppressed the $m = 1$ kink instability under all experimental conditions. Energy confinement times of $\tau_E \sim 15 \mu s$ were predicted during the 20 μs stable configuration. The peak temperature increased as the square of the current up to 110 eV with $\beta_\theta = 0.4-0.6$.

Experimentally stable RFP configurations were found in ETA-BETA (52,53) for currents up to 60 kA, whereas instabilities occurred at higher currents. Stable discharges were obtained for 10 μs containment times and plasma compressions of $x \sim 0.6$. The plasma was characterized by an average temperature of 10 eV and $\beta_\theta = 0.2-0.3$. Self-reversal has

also been exhibited using $x = 0.4-0.5$, yielding plasma decay times of 25-30 μs .

The ETL-TPE-1 (54,55) device has been run as a screw pinch and a RFP. Electron temperatures of ~ 10 eV were maintained for ~ 20 μs as β_0 rises above 0.6 when the column develops an $m = 1$ helical motion and touches the wall. Preliminary RFP operation of the STP (operated primarily as a high-beta tokamak) experiment has also showed improved stability using reversed-field programming (56).

The ZT-I experiment (57,58) was initially designed with a rapid current risetime, $\dot{I} \sim 1.4 \times 10^{12}$ A/S, using inductive energy storage with fuse interrupters. Ion temperatures of ~ 1 keV and electron temperatures of ~ 40 eV were obtained. Reversed-field programming was slow compared to the pinch time and completely stable MHD profiles were not obtained. Derating the device to currents of 40-70 kA and \dot{I} to 10^{11} A/S allowed field programming. The ion temperatures were decreased an order of magnitude and favorable stability was obtained. Confinement times of 10-15 μs resulted from the reversed-field programming compared to 3-4 μs with no reversed field. Loss of containment appeared to be caused by β_0 increasing above the stability limit (~ 0.5).

The major purpose of ZT-S is to examine confinement time scaling by increasing the bore from 10 cm on ZT-I to 15 cm on ZT-S. The confinement time is expected to scale as the field diffusion time, $\tau_f \sim r_w^2/D$, where D is the field diffusion coefficient. The confinement time was increased from 10-15 μs in ZT-I to 25-30 μs in ZT-S. The increased time scales approximately as the square of the minor radius.

These promising results have led to the proposal of many new experiments, which include (12) a 24-cm bore experiment (ETA BETA II, University of Padua, Italy) and a 40-cm bore device (ZT-40, Los Alamos Scientific Laboratory, Los Alamos, NM), both utilize field programming techniques. A 120-cm bore self-reversal experiment (RFX, Culham Laboratory, United Kingdom) is also planned. It is hoped that the above experiments will produce favorable scaling that will extrapolate to the reactor regime.

C. Reactor Studies

The few reactor studies that exist for the RFPR were done at the Los Alamos Scientific Laboratory in 1975 (13) and the Culham Laboratory at a low level of effort from 1969-1975 (59-61) leading to the much larger program presently in progress (62). All of these calculations use a steady-state plasma burn model (plasma temperature and density assumed constant throughout the burn) and were primarily interested in the plasma parameters necessary for a reactor with no consideration of the associated engineering; although, the present Culham program (62) will ultimately lead to a consistent engineering design.

Reactor calculations performed at Los Alamos (13) assumed the plasma is held at constant temperature (15 keV), poloidal beta ($\beta_{\theta} = 0.5$), and plasma compression ($x = 0.4$) for a specified time. The reactor power multiplication was assumed and plasma current limits were calculated based upon the total allowable neutrons incident on the first wall which will result in a specified first-wall lifetime.

Calculations performed at Culham used tokamak codes with appropriate RFPR resistivities and classical losses (59-61). In these studies MHD stability is determined by a limiting poloidal beta, $\beta_{OL} = 0.075 \Theta^3$ (63). This is a result of an increase in the shear of the fields as the plasma current is increased, and must not be used above $\Theta \sim 2$. This general trend of supporting more plasma pressure as the pinch moves away from the stabilizing wall is in opposition to the results obtained for configurations with the field shear already established. (Sec. II.A)

Using this limiting β_{OL} , when $\beta_{\Theta} < \beta_{OL}$ the behavior is assumed classical; when $\beta_{\Theta} > \beta_{OL}$ instabilities grow and supposedly saturate, appearing as enhanced loss mechanisms proportional to $\exp((\beta_{\Theta} - \beta_{OL})k)$. The value of k is sufficiently large for β_{OL} not to be exceeded by more than a few percent. For a 3-m device, $I = 25$ MA, $\Theta = 1.75$, and $n_i = 4 \times 10^{19} \text{ m}^{-3}$, the plasma ohmically ignites in 1.0 s. Cold particles are then injected to maintain the plasma temperature at 20 keV for 20 s. This steady-state system operates at $\beta_{\Theta} = 0.46$, and is achieved by the assumed turbulent loss mechanisms. The stability of the configuration during this process is difficult to assess. Energy balance calculations are not performed, although a thermal output of 2000 MW is calculated for an aspect ratio of 5.

The reactor study currently in progress at Culham (62) invokes the same postulated plasma loss mechanisms described above where an enhanced thermal conduction maintains a steady-state burn. For a 1.75-m device the parameters of the ohmically heated plasma (4.5 s heating phase for

$I = 19 \text{ MA}$) are $T = 10 \text{ keV}$, $n_i = 2.5 \times 10^{20} \text{ m}^{-3}$ and $\beta_\theta = 0.35$ during the 27.5 s burn phase resulting in a 30% fuel burnup. Using a full cycle of 40 s and normal conducting coils require a 42% recirculating electric power fraction resulting in a net output power of 600 MWe from a reactor of 16-m major radius at an estimated capital cost of \$2000/kWe.

III. DESCRIPTION OF ENERGY BALANCE

A. General Model

Evaluation of possible operating cycles for the RFPR requires a model of the reactor which allows a realistic energy balance. Such a model is shown schematically in Fig. (5). The plasma has an initial plasma energy W_{INT}^0 . The total stored energy W_{BO} is then transferred into the RFPR magnets and $W_{BO}(1-\eta_{ETS}) = W_{ETS}$ is assumed lost externally (outside of the magnet coil leads), where η_{ETS} is the magnetic energy transfer/storage efficiency. The remaining magnetic energy $W_{BO}\eta_{ETS}$ is partitioned between vacuum field energy, transport losses W_{TR} , eddy current losses in the blanket W_{EB} and magnet coil W_{EC} , ohmic heating energy W_{OHM} , and field energy trapped inside the plasma W_B^{IN} . The high- β plasma expansion restores some of the field energy by direct-conversion work W_{DC} . The plasma also produces neutron W_N , radiation W_{RAD} , conduction W_{COND} , internal plasma W_{INT} , and field W_B^{IN} energies which are thermally dissipated and eventually appear as thermal energy in the blanket. All of the field trapped in the plasma at the end of the burn W_B^{IN} is assumed to be thermally lost to the first wall. The blanket energy is then converted with a thermal efficiency η_{TH} to produce a gross electric energy W_{ET} . Auxiliary energy W_A requirements (pumps, plant operation, etc.), given as a fraction f_A of W_{ET} , complete the energy balance. Some fraction ϵ must be recirculated as makeup energy $W_C = \epsilon W_{ET}$, the net electric energy is then $W_E = (1-\epsilon)W_{ET}$, and the overall plant efficiency is $(1-\epsilon)\eta_{TH}$.

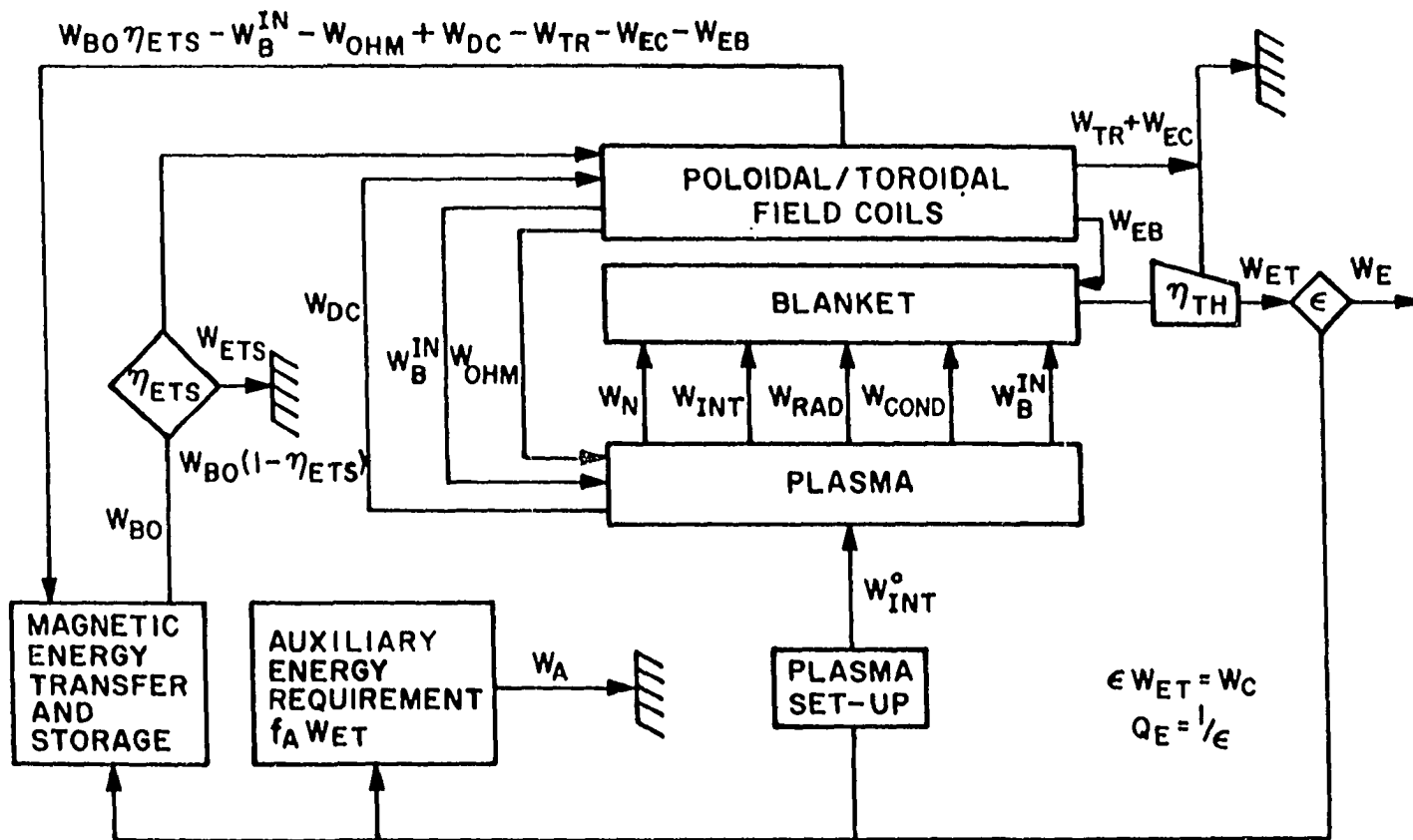


Fig. 5. Complete RFPR energy balance used in conjunction with a time-dependent RFP plasma model to evaluate a range of reactor operating points. Refer to text for notation.

An engineering Q-value Q_E is defined as

$$Q_E = \frac{W_{ET}}{W_C} = \frac{1}{\epsilon}$$

$$= \frac{\eta_{TH} \left[W_N + W_{INT} + W_{RAD} + W_{COND} + W_B^{IN} + W_{EB} \right]}{W_{INT}^O + W_{OHM} + W_B^{IN} + W_{TR} + W_{EB} + W_{EC} - W_{DC} + W_{ETS} + W_A} \quad (3.1)$$

and is used as a major performance indicator for the RFPR. Economic performance indicators have not been used to date, although ultimately economic considerations must be used to provide a final evaluation of a fusion power concept.

B. Plasma and Magnetic Field Models*

The radial dependence of both poloidal B_θ and toroidal B_z fields are assumed to be described by

$$B_\theta(r) = \begin{cases} A_\theta J_1(\alpha r), & r < r_p \\ \frac{\mu_0 I_z}{2\pi r}, & r > r_p \end{cases} \quad (3.2)$$

$$B_z(r) = \begin{cases} A_z J_0(\alpha r), & r < r_p \\ B_R, & r > r_p \end{cases} \quad (3.3)$$

*MKS units are used throughout, although plasma temperature is expressed in keV units, $kT \text{ (J)} = T \text{ (keV)} \times 10^3 e$, where $e = 1.602 \times 10^{-19} \text{ J/eV}$.

where $J_0(\alpha r)$ and $J_1(\alpha r)$ are Bessel functions of the first kind, A_θ and A_z are constants to be determined, $\mu_0 = 4\pi \times 10^{-7}$ H/m, I_z is the toroidal plasma current, and B_R is the uniform toroidal field outside the plasma. The good agreement between the assumed fields and actual MHD stable field profiles (13) is shown in Fig. (6), which gives the radial dependence of B_θ and B_z .

Toroidal flux conservation is assumed inside the plasma, which implies that the initial toroidal flux ($\pi r_w^2 B_{z0}$) must equal $B_z(r)$ integrated over the plasma area ($2\pi r dr$). Performing the integration gives

$$A_z = \frac{\alpha r_p B_{z0}}{2 x^2 J_1(\alpha r_p)} \quad (3.4)$$

where x is the plasma radius r_p divided by the wall radius r_w , and B_{z0} is the initial toroidal field. The radius of the plasma is taken as the point of zero B_z field for $x < 1$ ($\alpha r_p = 2.405$), and α must be determined for $x = 1$.

From Maxwell's equations, assuming a static electric field,

$$\mu_0 \vec{j} = \vec{\nabla} \times \vec{B} \quad , \quad (3.5)$$

the plasma current densities are given by

$$j_z(r) = \frac{\alpha A_\theta J_0(\alpha r)}{\mu_0} \quad (3.6)$$

$$j_\theta(r) = \frac{\alpha A_z J_1(\alpha r)}{\mu_0} \quad . \quad (3.7)$$

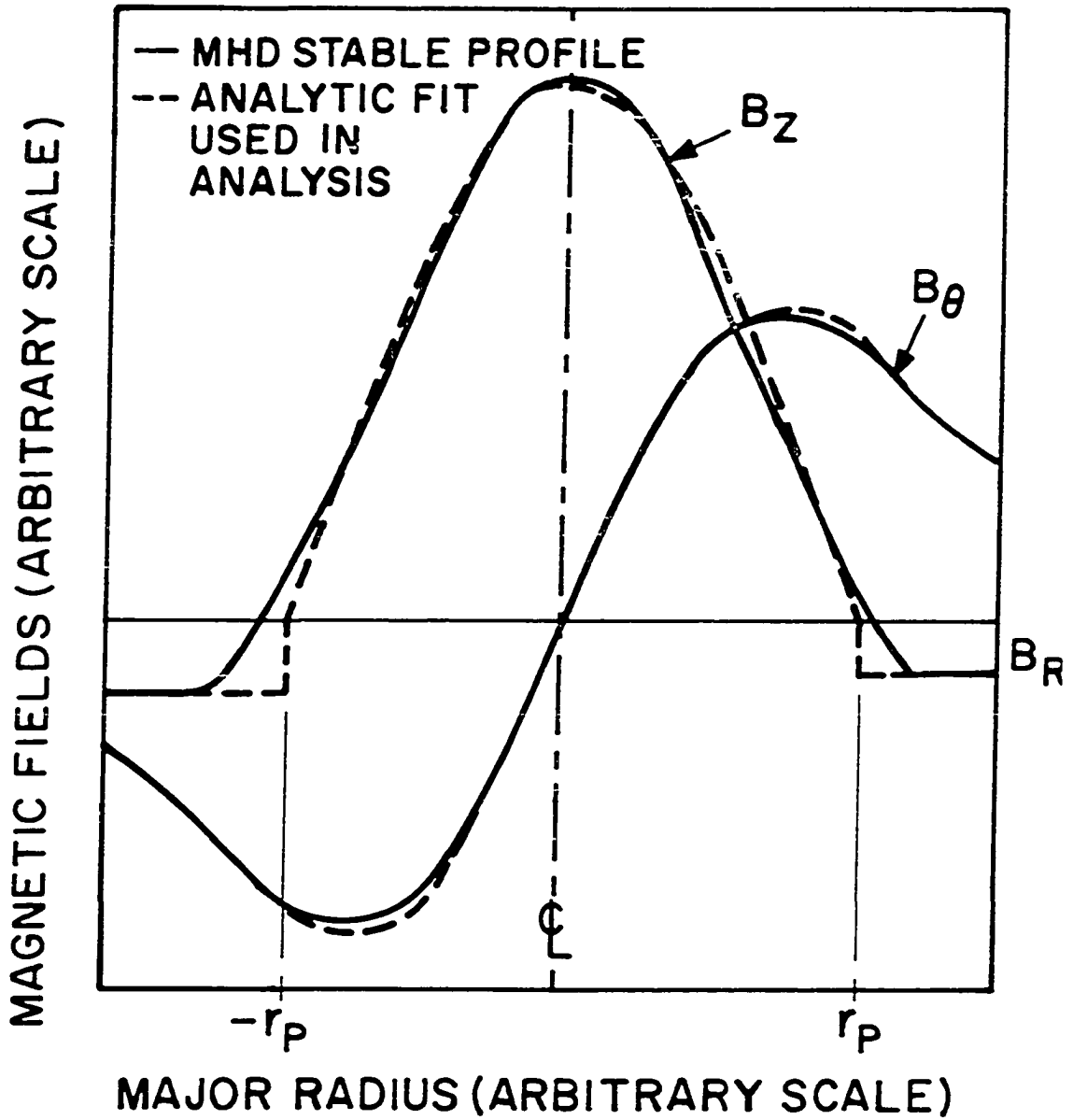


Fig. 6. Comparison of assumed poloidal B_θ and toroidal B_z fields and actual MHD stable field profiles (13).

The toroidal plasma current I_z must equal the integral of j_z over the plasma cross section, which leads to

$$A_\theta = \frac{\mu_0 I_z}{2\pi r_p J_1(\alpha r_p)} \quad (3.8)$$

From Maxwell's equations (static electric field) the pressure balance is given by

$$\frac{1}{\mu_0} (\vec{\nabla} \times \vec{B}) \times \vec{B} = \vec{\nabla} p(r) \quad (3.9)$$

Substituting the magnetic fields into Eq. (3.9) and integrating over the plasma radius gives the plasma pressure as a function of radius

$$p(r) = \frac{A_\theta^2 - A_z^2}{2\mu_0} \left[J_0^2(\alpha r) - J_0^2(\alpha r_p) \right] \quad (3.10)$$

Within the constraints of the global (zero-dimensional) plasma model use of the average integrated plasma pressure is desirable. Integrating Eq. (3.10) over the plasma area gives

$$p = \frac{p(r)}{J_0^2(\alpha r) - J_0^2(\alpha r_p)} J_1^2(\alpha r_p) \quad (3.11)$$

The average plasma pressure p is given by a summation of nkT over all plasma species, where an isothermal plasma is generally assumed. Substituting Eq. (3.10) into Eq. (3.11) and utilizing the expressions for A_θ and A_z gives

$$p = \frac{1}{2\mu_0} \left[\frac{I_z^2 \mu_0^2}{(2\pi r_p)^2} - \frac{B_{z0}^2 (\alpha r_p)^2}{4x^4} \right] \quad (3.12)$$

For $x = 1$, Eq. (3.12) is solved for α which defines the field and pressure profiles during the initial current rise.

A poloidal beta β_{θ} is defined as the average plasma pressure divided by the poloidal field pressure at the plasma radius r_p which gives

$$\beta_{\theta} = \frac{p}{B_{\theta}^2/2\mu_0} = \frac{A_{\theta}^2 - A_z^2}{A_{\theta}^2} \quad (3.13)$$

This expression is used to monitor stability criteria during the thermonuclear burn.

C. Plasma Energy Balance

The time-rate-of-change of plasma energy is

$$\frac{d(3p\pi r_p^2/2)}{dt} = P_{\alpha} + P_{\text{OHM}} - P_{\text{RAD}} - P_{\text{COND}} - P \frac{d(\pi r_p^2)}{dt} \quad (\text{W/m}), \quad (3.14)$$

where the per meter powers are alpha-particle, ohmic, radiation, and thermal conduction. The last term in Eq. (3.14) represents direct-conversion work done by high- β plasma expansion against confining magnetic fields. Substituting Eq. (3.12) into Eq. (3.14), and solving for dx/dt gives

$$\frac{dx}{dt} = \frac{\frac{P_{\alpha} + P_{\text{OHM}} - P_{\text{RAD}} - P_{\text{COND}}}{\pi r_p^2} - 3 \frac{B_{\theta}^2}{2\mu_0} \frac{1}{I_z} \frac{dI_z}{dt}}{\frac{1}{x} \left[\frac{3}{2\mu_0} \frac{B_{z0}^2}{x^4} \frac{(2.405)^2}{4} + 2p \right]}, \quad (3.15)$$

where B_{θ} is defined at the plasma radius r_p .

The spatially dependent alpha-heating power ($\propto n^2$) is numerically integrated over the plasma area using Eq. (3.11) and assuming an isothermal plasma. The result is

$$P_\alpha = 5.64 \times 10^{-13} n_D n_T \langle \sigma v \rangle A \quad (3.16)$$

where n_D and n_T are the spatially averaged deuterium and tritium number densities, and A is approximated by an analytic function (within 1% accuracy) given by

$$A = \begin{cases} \left[1.333 + 0.039 \alpha_{r_p} \left(1 + 0.21 (\alpha_{r_p})^4 \right) \right] \pi r_p^2 & , x = 1 \\ 2.098 \pi r_p^2 & , x < 1 \end{cases} \quad (3.17)$$

Bremsstrahlung, line, and cyclotron radiation contribute to the radiation power P_{RAD} . Impurity radiation is incorporated for oxygen and utilizes fitted functions given in Ref. 64. The average bremsstrahlung power is (18)

$$P_{\text{BR}} = 5.35 \times 10^{-37} n_e^2 Z_{\text{eff}} T_e^{1/2} A \quad (3.18)$$

where Z_{eff} is the sum of $n_k z_k^2$ divided by the sum of $n_k z_k$ over all ion species k . The cyclotron radiation leaving a nonabsorbing plasma (18) is numerically integrated over the plasma cross section for $\alpha_{r_p} = 2.405$ to give

$$P_{\text{cy}}^T = 6.20 \times 10^{-17} n_e \bar{B}^2 T_e \left(1 + \frac{T_e}{204} \right) \pi r_p^2 \quad , \quad (3.19)$$

where an effective magnetic field \bar{B} has been defined as

$$\bar{B}^2 = \frac{2.098}{3} \left[B_{\theta}^2 + 3 \frac{(2.405)^2 B_{z0}^2}{4x^4} \right] . \quad (3.20)$$

The poloidal field B_{θ} is evaluated at the plasma radius. The fraction of P_{CY}^T leaving the plasma, accounting for absorption and assuming non-reflecting walls, is (18)

$$k_L = 2.1 \times 10^{-3} T_e^{7/4} \left[\frac{c\bar{B}\epsilon_0}{2r_p n_e e} \right]^{1/2} \quad (3.21)$$

The fraction of P_{CY}^T leaving the plasma when plasma absorption and a reflecting cylindrical first wall is present is given as k_C in Ref. 65. Thus, given a first wall with a fraction f formed by holes, the cyclotron radiation power leaving the plasma and escaping through these holes is $P_{CY}^H = P_{CY}^T k_L f$. The power leaving the plasma and absorbed by the first wall is $P_{CY}^W = P_{CY}^T k_C (1-f)$ for a reflecting metallic wall and $P_{CY}^W = P_{CY}^T k_L (1-f)$ for a nonreflecting wall. The total power leaving the plasma is $P_{CY} = P_{CY}^H + P_{CY}^W$. In this study a low- z ceramic coating (Al_2O_3) on the first wall is taken to be nonreflecting.

The ohmic heating power P_{OHM} is first calculated for $\alpha r_p = 2.405$. From Eqs. (3.5,9), the current perpendicular to B must support the plasma pressure or

$$j_{\perp}(r)B(r) = \frac{\partial p(r)}{\partial r} , \quad (3.22)$$

and the remaining current is directed parallel to field lines

$$j_{\parallel}(r) = (j_z^2 + j_{\theta}^2 - j_{\perp}^2)^{1/2} . \quad (3.23)$$

Numerically integrating the ohmic heating power $(\eta_{\parallel} j_{\parallel}^2(r) + \eta_{\perp} j_{\perp}^2(r))$ over the plasma cross section, and fitting the result to an analytic function (within 1% accuracy) gives

$$P_{\text{OHM}} = \frac{I_z^2}{\pi r_p^2} \left(\frac{2.405}{2} \right)^2 \left\{ \eta_{\parallel} (2 - \beta_{\theta}) + (\eta_{\perp} - \eta_{\parallel}) \beta_{\theta}^2 \right. \\ \left. \left[1 - 1.13(1 - \beta_{\theta})^{1/2} + 0.43(1 - \beta_{\theta}) \right] \right\}, \quad (3.24)$$

where the plasma resistivities are assumed classical and are given in the Appendix. During the early startup phase ($\alpha r_p < 2.405$), the relatively cool plasma yields $\beta_{\theta} \sim 0$, and only the parallel resistivity need be considered. The integrable ohmic heating power is then

$$P_{\text{OHM}} = 2 \eta_{\parallel} \frac{I_z^2}{\pi r_w^2} \left(\frac{\alpha r_w}{2} \right)^2 \left[1 + \left(\frac{J_0}{J_1} \right)^2 \left(1 - \frac{1}{\alpha r_w} \frac{J_1}{J_0} \right) \right]. \quad (3.25)$$

Conductive losses from the plasma can be properly treated as a function of time by a one-dimensional MHD code. Such a calculation is beyond the scope of this study and an approximate expression is used to describe the dominant ion thermal conduction losses. The conductive power loss is taken as

$$P_{\text{COND}} = K_{\perp} (\partial T / \partial r) 2\pi r_w = 4\pi T_i K_{\perp} \quad (3.26)$$

where T is taken as $(1 - r^2/r_w^2) T_i$ (steady-state solution for an infinite circular cylinder with uniform properties) and the thermal conductivity

K_{\perp} is given in the Appendix. This power loss term is generally very small and has no impact on the energy balance.

D. Magnetic Energy Storage and Joule Losses

The toroidal and poloidal fields in the plasma and between the plasma and the coil are given by Eqs. (3.2, 3). The respective field profiles in the coil are given by

$$B_{\theta}(r) = \frac{\mu_0 I_z}{2\pi r} \frac{\delta_p^2 - \left(\frac{r}{r_{cp}}\right)^2}{\delta_p^2 - 1} \quad (3.27)$$

$$B_z(r) = - B_R \frac{r_{cz}}{\Delta r_{cz}} \left(\delta_z - \frac{r}{r_{cz}} \right) , \quad (3.28)$$

where r_{cp} is the inside radius of the coil, Δr_{cp} is the coil thickness, $\delta_p = 1 + \Delta r_{cp}/r_{cp}$, and the toroidal coil parameters are defined in an analogous manner. The dependence of B in the coil assumes a uniform current density (i.e. fully litzed and transposed windings). Integrating $(B^2 2\pi r dr)/2\mu_0$ over each region (assuming the poloidal energy stored in the iron core is negligible) results in the following expressions for the energy stored in the RFPR:

$$W_{B\theta}(\text{J/m}) = \frac{\mu_0 I_z^2}{4\pi} \left[\left(\frac{1}{2} - \frac{J_o}{\alpha r_p J_1} + \frac{J_o^2}{2J_1^2} \right) + \ln\left(\frac{r_{cp}}{r_p}\right) + \frac{\delta_p^4 \left(\ln \delta_p - \frac{3}{4} \right) + \delta_p^2 - \frac{1}{4}}{(\delta_p^2 - 1)^2} \right] \quad (3.29)$$

$$\begin{aligned}
W_{Bz} \text{ (J/m)} &= \frac{B_{z0}^2}{2\mu_0} \frac{(\alpha r_p)^2 \pi r_p^2}{4x^4} \left[1 + \frac{J_0^2 (\alpha r_p)}{J_1^2 (\alpha r_p)} \right] \\
&+ \frac{B_R^2}{2\mu_0} \pi r_z^2 \left[\left(1 - \frac{r_p^2}{r_{cz}^2} \right) + (\delta_z - 1) \left(\frac{1}{6} \delta_z + \frac{1}{2} \right) \right]. \quad (3.30)
\end{aligned}$$

The first, second, and third terms for both fields are, respectively, the energy stored in the plasma, between the plasma and the coil (i.e. in the vacuum region and blanket structure), and in the coil, per se.

A uniform poloidal current distribution is assumed around the minor radius of the torus. The required distribution for stability and equilibrium must ultimately be determined by a MHD calculation. The coil transport is then

$$P_{TRG} \text{ (W/m)} = \frac{\eta_{cp}}{\pi \left[(r_{cp} + \Delta r_{cp})^2 - r_{cp}^2 \right] \lambda_{cp}} I_z^2, \quad (3.31)$$

where η (ohm-m) is the coil electrical resistivity and λ is the filling fraction of conductor in the coil. The transport losses in the toroidal field coil are expressed as

$$P_{TRZ} \text{ (W/m)} = \frac{\eta_{cz} 2\pi (r_{cz} + \Delta r_{cz}/2)}{\Delta r_{cz} \lambda_{cz}} \frac{B_R^2}{\mu_0}. \quad (3.32)$$

Parallel plate leads are assumed where the thickness of one plate is p_t and a gap between the plates is p_g , so that the total lead thickness

is $2p_t + p_g$. Specifying the lead width p_w , lead length p_ℓ , and length of coil fed by lead as ℓ , the energy storage and transport losses are

$$W_{\text{BLD}} \text{ (J/m)} = \frac{B_L^2}{2\mu_0} \frac{p_w p_\ell}{\ell} \left[p_g + \frac{2}{3} p_t \right] \quad (3.33)$$

$$P_{\text{TRLD}} \text{ (W/m)} = \frac{2 p_\ell p_w}{p_t \lambda \ell} \frac{B_L^2}{\mu_0^2} \quad , \quad (3.34)$$

where N is the turns ratio, λ is the fraction of conductor in the lead, η is the resistivity and

$$B_L = \frac{\mu_0 I_z}{p_w N_{\text{CP}}} \quad , \quad (3.35)$$

$$B_L = \frac{\ell B_R}{p_w N_{\text{CZ}}} \quad , \quad (3.36)$$

for the poloidal and toroidal coils, respectively.

Eddy current losses in the coils are incurred during the current rise and fall corresponding to a total time of $2\tau_R$. Taken as a fraction of the transport losses incurred during the plasma burn τ_B , these losses are estimated to be (66)

$$\frac{W_{\text{EC}}}{W_T} \sim 0.02 n^2 \left(\frac{d}{\delta} \right)^4 \frac{\tau_R}{\tau_B} \quad (3.37)$$

The n layers of thickness d constitute a coil of total thickness nd/λ having an electrical skin depth of $\delta = (0.5 \times 10^6 \eta \tau_R)^{1/2}$. Using room temperature copper ($\eta = 1.8 \times 10^{-8} \Omega\text{-m}$), $\tau_R = 0.1$, $\tau_R/\tau_B = 0.1$,

$d = 0.007$, $n = 100$, $\lambda = 0.7$ gives a total coil thickness of 1 m and $W_{EC}/W_{TR} \sim 0.05$.

Eddy current losses (66) in the lithium blanket containing a fraction f_w of the total stored energy W_{BO} are

$$\frac{W_{EB}}{W_{BO}} \sim f_w \frac{\pi h^2}{20 \delta^2} \quad (3.38)$$

for segments of width h . For lithium at 1000 K ($\eta \sim 2 \times 10^{-6} \Omega\text{-m}$), $f_w \sim 0.05$ (0.15 m lithium length in blanket), $h = 0.1$ m, the losses are $W_{EB}/W_{BO} \sim 0.001$.

The eddy current losses are then taken as 5% of the transport losses for a coil constructed of 7 mm layers, plus 0.1% of W_{BO} for a segmented 10 cm blanket. These quantities are used for all parameter studies and may be achieved by adjusting the thickness indicated above.

E. Computational Procedure

The initial bias field B_{z0} is calculated from Eq. (3.12) based upon a desired minimum plasma compression x_m . The value of αr_p is then calculated from Eq. (3.12) as the current rises sinusoidally, which defines the field profiles. When αr_p reaches 2.405, a numerical integration of Eq. (3.15) gives the plasma radius variation.

Alpha particle heating is treated by a Fokker-Planck calculation (67), which allows for the possible non-Maxwellian phase-space distributions for both electron and fuel ion species. The addition of particles to the alpha-particle distribution function is given by

$$\Delta F_{\alpha} (n/v^3) = \frac{\Delta n_{\alpha}}{\sqrt{\pi} \Delta_d (4\pi v_{\alpha}^2)} e^{-\left(\frac{v-v_{\alpha}}{\Delta_d}\right)^2} \quad (3.39)$$

where v_{α} is the velocity corresponding to the 3.52 MeV alpha particle, Δn_{α} is the number density of alphas added at each time step Δt , and the doppler broadening due to the background ion species is $\Delta_d = (kT_i/2m_i)^{1/2}$.

During each time step the electron temperature is adjusted according to the varying plasma volume and plasma powers P_{OHM} and P_{RAD} . Similarly, the ion temperatures must reflect the volume change and power loss P_{COND} . At the end of each time step the alpha velocity distribution is modified to account for plasma expansion, and the energy equipartition between plasma species is followed by the Fokker-Planck calculation. Numerically integrating plasma powers and coil transport losses completes the energy balance calculation.

IV. RESULTS

A. Reactor Startup Phase

Establishing the field profiles necessary for stable operation of an RFPR appears to be a formidable problem. The initial constant toroidal field B_{z0} and increasing current results in a field configuration similar to that in a tokamak. This q-stabilized system must then be transformed into a RFP by proper programming of the fields. The achieving of stability during this phase seems unlikely, and turbulence similar to that exhibited by tokamaks may result. Pressure balance is assumed, however, and the approximate field profiles during startup are modeled by the equations in Section III. This startup sequence is one of the major uncertainties in the reactor design.

Preionization is assumed to be achieved uniformly to a density of $n_e = 10^{-6} n_0$ by a RF-heating source (64,68). The electric field applied to the plasma by the homopolar machine must then be sufficient to sustain breakdown. This electric field is taken as $I R_p / (2\pi R)$ where R_p is the resistance of the plasma. This ignores the inductive spike ($\sim 1 \mu\text{sec}$) at time $t \rightarrow 0$ when the plasma current is near zero (64). The minimum field for breakdown is $\sim 5 \text{V/m-mTorr}$ for densities above $\sim 0.5 \text{ mTorr}$ for reactors with a minor radius on the order of a meter (64,68). Electron runaway is observed (69-71) above 20 V/m-mTorr which may be taken as a maximum allowable field (64,68). When a significant fraction of the neutral population is ionized ($\sim 10\%$) electron-ion collisions dominate and determine the conditions for electron runaway. A critical electric field $E_c = 1.6 \times 10^{-11} n_e n_{ii} T_e^{1/2}$ (72) divided by the

electric field imposed on the plasma $E = \eta_{||} I_z / \pi r_p^2$ gives $E_c/E = 2 \times 10^{-7} (N_e \beta_0)^{1/2}$, where the line density N_e and pressure balance is used. Having $E_c/E > 50$ results in an insignificant loss due to runaway electrons (72). Very low β_0 values result during the low plasma temperatures at startup, however, the initial 20 V/m-mTorr is then the limiting constraint. Electron runaway at higher temperatures is apparently not a problem. Taking typical values of $N_e \sim 10^{21} \text{ m}^{-1}$ and $\beta_0 \sim 0.01$ (during startup) gives $E_c/E \sim 630$.

Assuming the aforementioned preionization, plasma breakdown is then modeled with a tokamak startup code (64) until the plasma temperature reaches ~ 0.1 keV. The discharges are typically started at relatively low densities (~ 0.5 - 1 mTorr) which minimizes the power loss due to line radiation at low temperatures (~ 0.01 keV). The line radiation power is proportional to $n_e n_{im}$ (n_{im} is the impurity number density), and may be difficult to overcome if the initial density is too high. The final density is then achieved by gas injection after the resonance line radiation of low-Z impurity ions has decreased. For oxygen the peak resonance occurs at ~ 0.01 keV, and neutral gas is allowed to flow into the system for $T > 0.02$ keV until the required density is achieved.

Only with further laboratory experimentation using large radius plasmas and long startup times (~ 0.1 s) can the true behavior of the plasma during the initiation phase be seen. The scheme used herein provides an estimate of plasma parameters and powers during the startup phase.

B. Thermonuclear Burn Cycles

The pressure balance equation (Eq. (3.12)) is plotted on the P-V diagram in Fig. (7), which is used to illustrate the operational modes and limitations anticipated for pulsed, high- β operation. The dependence of β_0 with respect to x is also given by Eq. (3.12) as $\beta_0 = 1 - (x_m/x)^2$ where a constant I_z current and negligible plasma pressure at $x = x_m$ is assumed. Starting at $x = 1$ the plasma is compressed to $x = 0.4$, which is taken as the minimum stable plasma radius (29-31). Ohmic heating rapidly brings the plasma to ignition. Noting from Fig. (7) that all solid curves pertain to lines of constant I_z current throughout the burn, alpha-particle heating subsequently raises the plasma pressure to a maximum at $x^2 = 0.32$ corresponding to $\beta_0 = 0.5$. The plasma continues to heat and expands to the wall. The inside toroidal field B_{zI} reversibly increases to a maximum at $x^2 = 0.16$ and then decreases according to the laws of flux conservation. The direct-conversion work W_{DC} associated with plasma expansion against the magnetic field is given by the area enclosed by the plasma pressure-volume curve. Stable profiles are known to exist up to $\beta_0 \sim 0.58$, but as the hot plasma continues to expand to the wall, β_0 continues to rise to a maximum of $\beta_0 = 0.84$ at $x = 1$.

To remedy this unstable situation, the plasma pressure must be much lower before expansion to the wall occurs. For a constantly rising plasma temperature the B_0 field must be decreased before the plasma nears its maximum pressure. This case, denoted by the dashed curves, indicates that the direct-conversion work is now compromised and the

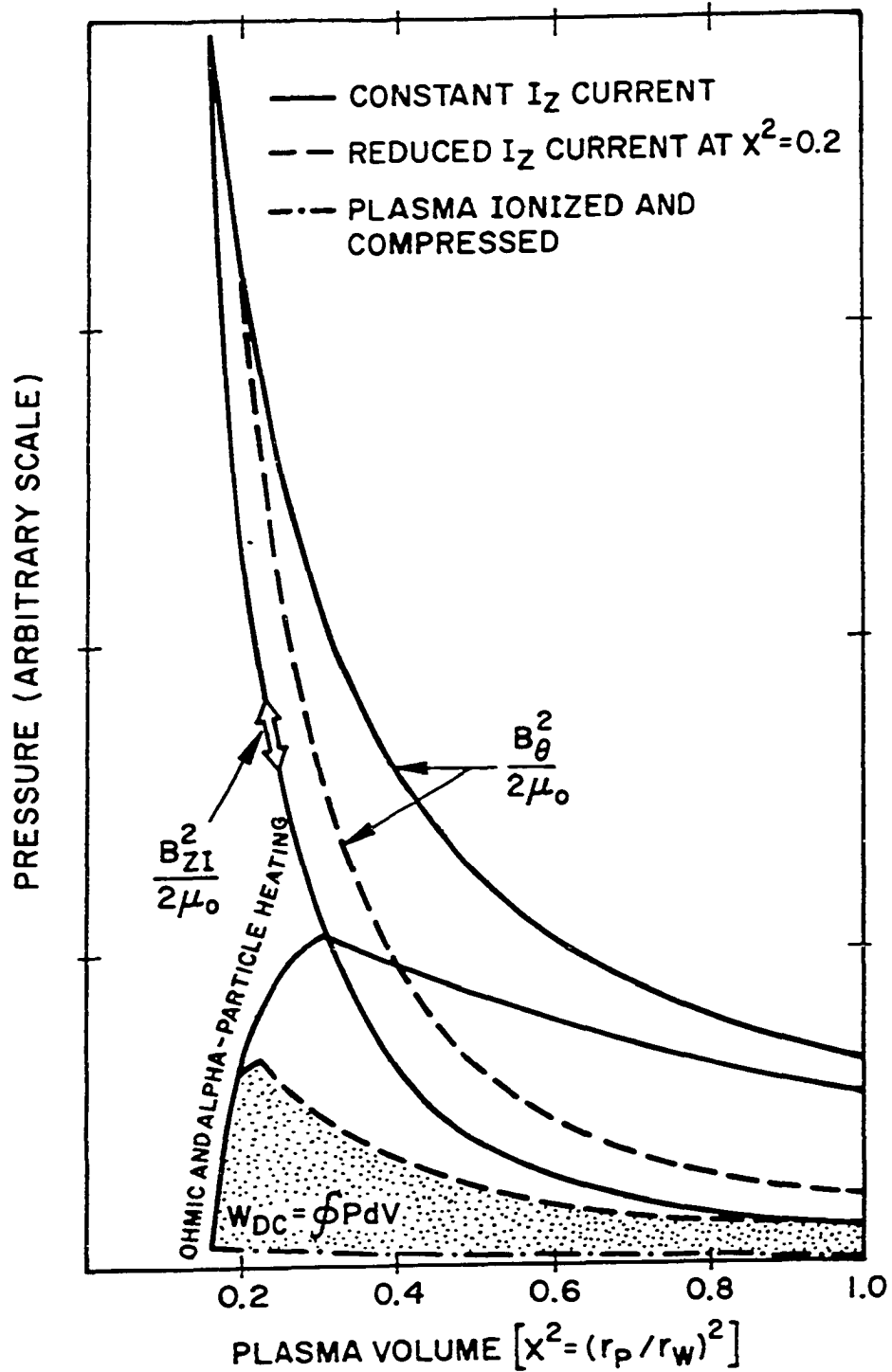


Fig. 7. Generalized pressure-volume diagram for the RFPR. Magnetic field pressures, plasma pressure p , and the plasma direct-conversion work W_{DC} for high-beta plasma expansion against a magnetic field are shown for the assumed sharp-boundary plasma model.

lower average plasma β will result in a lower power output. However, if the plasma temperature can be controlled, then the plasma pressure can be brought to $\beta_0 \sim 0.5$ and maintained at that point throughout the burn. Near the end of the burn the plasma temperature is decreased, giving a lower β_0 and permitting the dashed curves to be followed; a stable plasma ($\beta_0 \leq .58$) results as it expands to the wall.

The dynamic plasma and energy-balance models described in Sec. III were used to perform a parametric systems analysis of a wide range of RFPR burn cycles. The engineering Q-value Q_E served as the object function for this system optimization. Reactor dimensions used in this study are summarized in Table 2. The initial plasma conditions (temperature, D-T ratio, filling pressure), initial toroidal bias field, magnitude and wave form of the toroidal current and the total burn time were varied over a wide parameter range. The magnitude of the first-wall temperature rise and associated thermal stresses, both of which were computed as a function of time by the RFP systems model, and the total plasma beta were continually monitored and used as major constraints. The toroidal current I_z was increased sinusoidally with a rise time τ_R , held constant (crowbarred) for a time τ_B , and then was sinusoidally decreased with a fall time equal to τ_R .

For a 50%-50% D-T fuel mixture the plasma ignites and can reach $\beta_0 \sim 0.35$ before the plasma must be expanded to the walls; plasma expansion occurs with a half-cycle fall time approximately 10% that of the burn time. This scenario maintains a stable plasma ($\beta_0 < 0.5$) throughout the burn cycle. The initial filling pressure is varied until

Table 2. Dimensions used in RFPR energy-balance study

Symbol	Definition	Value	
r_w	first-wall radius (m)	variable	
	first-wall Nb-1%Zr thickness (m)	0.002(0.005) ^a	
	first-wall Al ₂ O ₃ coating thickness (m)	3.0×10^{-4}	
	blanket thickness (m)	0.4	
		Toroidal	Poloidal
r_c	inside coil radius (m) ^b	$r_w + 0.4$	$r_{cz} + \Delta r_{cz}$
Δr_c	coil thickness (m)	0.15(0.25)	0.60(1.0)
N_c	number of turn coil	15	1
P_l	parallel plate lead length (m)	5.0	5.0
P_w	parallel plate lead width (m)	0.13	$2\pi r_{cp}$
P_t	parallel plate thickness (m)	Δr_{cz}	Δr_{cp}
P_g	gap between parallel plates (m)	0.01	0.01
l	length of device fed by leads (m) ^c	2.0	$10\pi r_w$
λ	fraction of conductor in coil and leads	0.7	0.7
η	resistivity (copper) of coil and leads (ohm-m)	1.8×10^{-8}	1.8×10^{-8}

^aDimensions in parentheses used for the longer burn times associated with the case which controls β_θ by D-T burnout (90%-10% D-T fuel mixture).

^bThe subscripts z and p are added to denote the toroidal and poloidal field systems, respectively.

^cAspect ratio taken to be 5.0.

the maximum Q_E is obtained. In Fig. 8 the first-wall radius r_w versus the average maximum toroidal current density \hat{j}_z is shown as a function of Q_E for the 50%-50% D-T fuel mixture case (β_0 control by early quench). Superimposed upon the Q_E curves are lines of constant first-wall surface temperature rise ΔT_w (K) where the first wall (0.3 mm) Al_2O_3 / (2 mm) Nb-1Zr is cooled by a stagnant pool of lithium.

Attempting to achieve higher values of Q_E , plasma temperature control using cold fuel injection or impurity addition was considered, but the alpha-heating power must be balanced by losses to the first wall in order to maintain a constant plasma temperature. Since the alpha-heating power is ~ 28 times that of bremsstrahlung radiation at 20 keV, the surface heat flux to the wall would be correspondingly increased. For typical initial ion densities (50%-50% D-T fuel mixture, 2-m first-wall radius, and $\hat{j}_z = 20 \text{ MA/m}^2$) of $1.4 \times 10^{20}/\text{m}^3$ compressed to $8.6 \times 10^{21}/\text{m}^3$ at the minimum compression $x = 0.4$, a heat removal rate of $\sim 10 \text{ MW/m}^2$ at the first wall would be necessary to achieve a constant plasma temperature 20 keV. This exceedingly high surface heat flux would be intolerable over the 1.14 s burn time anticipated for the aforementioned case. The actual bremsstrahlung power $\sim 0.3 \text{ MW/m}^2$ produces a 163 K degree surface temperature rise for a (0.3 mm) Al_2O_3 / (1 mm) Nb-1Zr first wall. For these methods of plasma temperature control, the plasma density must be decreased by ~ 5 to lower the alpha-heating power a factor of 25; a corresponding increase in burn time would result. The potential technical difficulties associated with the injection of cold fuel or impurities and questions of plasma

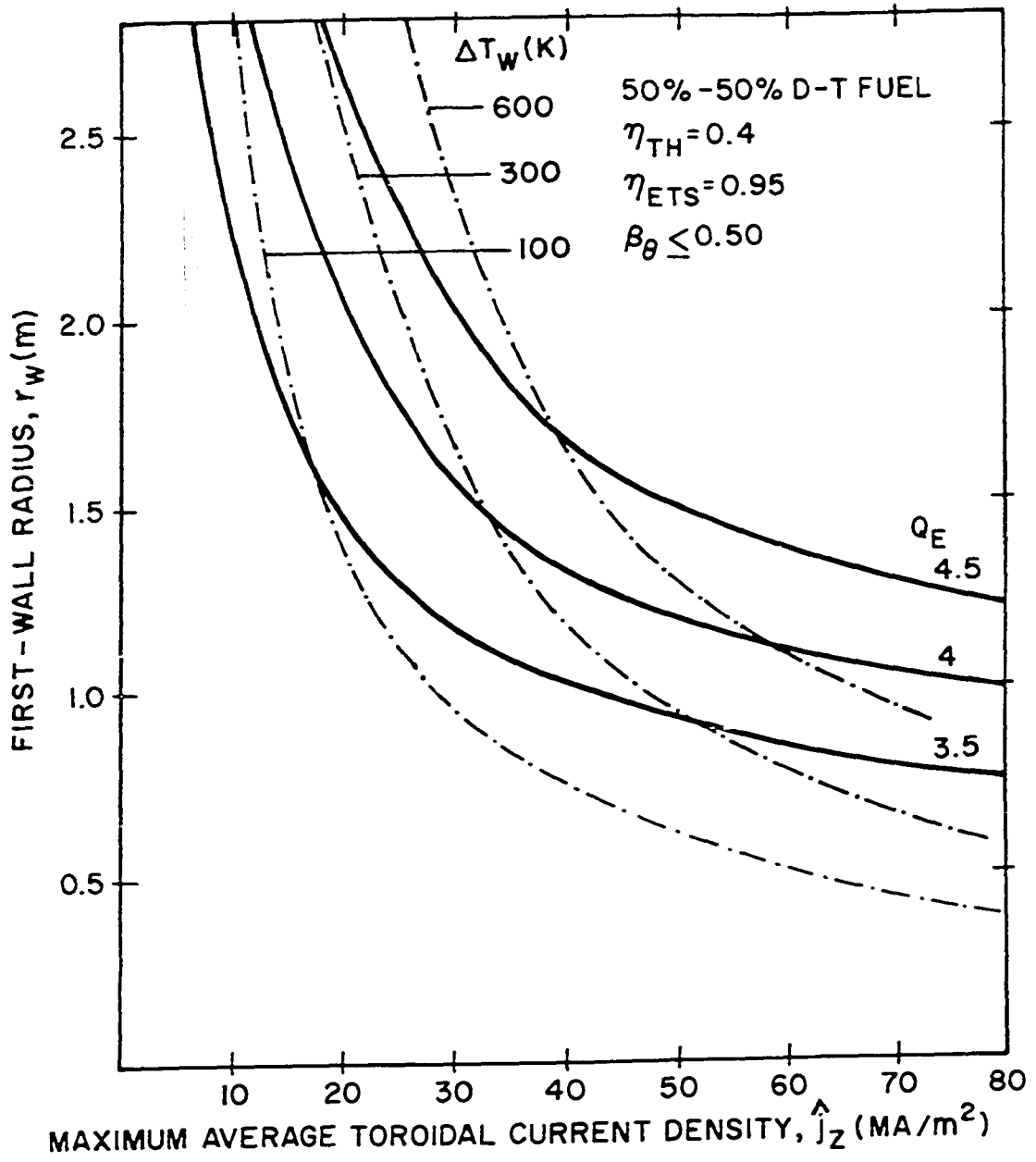


Fig. 8. Lines of constant Q_E for various first-wall radii r_w and maximum average toroidal current densities \hat{j}_z (solid curves) where a 50%-50% D-T fuel mixture is used. The dotted-dashed curves are lines of constant first-wall ((0.3 mm) Al₂O₃/(2 mm) Nb-1Zr) surface temperature rise ΔT_w (k).

stability incurred by the use of such processes were also major factors leading to the decision not to utilize injection techniques for plasma temperature control.

A method of temperature control utilized in this study lowers the initial tritium loadings below 50%. Through this scheme, the plasma provides automatic temperature control by tritium burnup, decreased alpha-particle heating, and natural radiative losses. In Fig. 9 Q_E versus the initial tritium fraction f_T is shown for a first-wall radius of 2 m and maximum average toroidal plasma current density $\hat{j}_z = I_z/\pi (r_w x_m)^2 = 15 \text{ MA/m}^2$. The plasma is expanded to the wall after 90% of the available tritium has been consumed. The half-cycle rise and fall time of I_z was taken to be 0.1 s. The filling pressure P_A is varied until $(\beta_\theta)_{\text{MAX}} \sim 0.43$ before expansion, resulting in $\beta_\theta \sim 0.5$ at the first wall after expansion. Shown in Fig. 9 are the required filling pressures, associated burn times and maximum ion temperatures for each initial tritium fraction f_T . As the tritium fraction f_T is increased, high ion temperatures result in a reduction of the alpha-particle heating power ($P_\alpha \sim \langle \sigma v \rangle_{DT}/T^2$ decreases by one e-fold of the peak value at $T = 50 \text{ keV}$). Much longer burn times, therefore, are required to achieve high burnups at higher ion temperatures. The plasma temperature reaches $T = 50\text{--}60 \text{ keV}$ for $f_T = 0.08\text{--}0.10$ and since the burn times are greatly increased beyond $f_T = 0.1$ and Q_E is not, $f_T = 0.1$ is chosen. Longer burn times at high ion temperatures results in higher coil transport losses and a decreasing thermonuclear output, respectively, thereby resulting in the saturation and eventual decrease in Q_E as f_T is

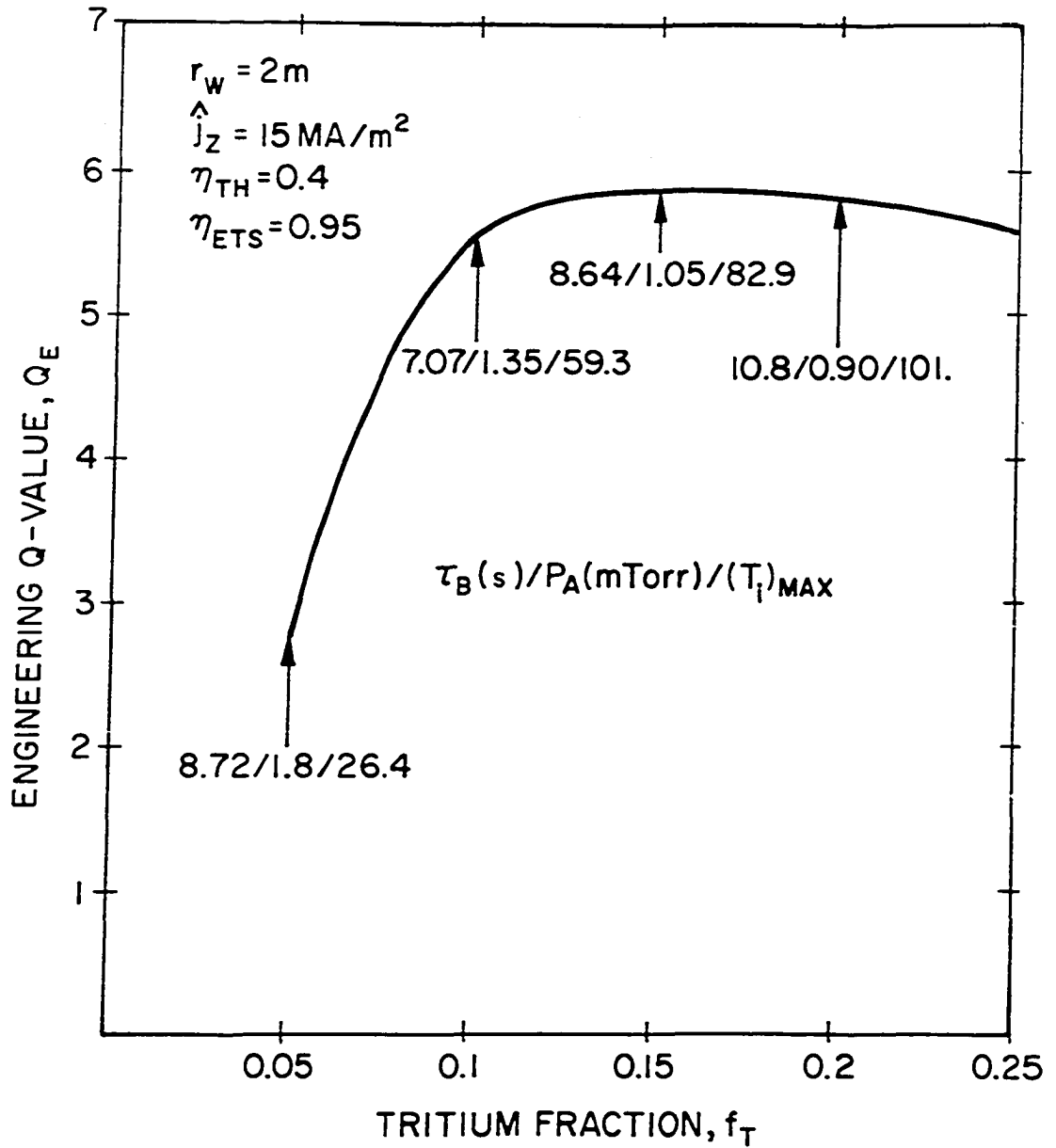


Fig. 9. Dependence of the engineering Q-value Q_E on the initial plasma tritium fraction f_T for 90% burnup of the available tritium in the plasma.

increased. In Fig. (10) curves of constant Q_E and first-wall temperature rises are shown for the 90%-10% D-T fuel mixture case (β_θ control by tritium burnout) using a thicker first wall (0.3 mm) Al_2O_3 / (5 mm) Nb-Izr (Table 2) and increased thickness of the magnet coil (from 0.6 to 1.0 m). The longer burn times associated with the lower tritium loadings necessitate thicker first walls to maintain approximately the same temperature drop across the wall (a measure of the internal mechanical stress, typically < 50 K) and bulk temperature rise. The joule losses in the coil are also increased by the longer burn times and are offset by the thicker coil. Increasing the coil thickness increases Q_E but the trade-off between coil size, complexity and cost versus higher Q_E must eventually be considered.

C. Plasma Quench

At the end of the burn the I_z current is lowered sinusoidally with a half-cycle fall time τ_R and the plasma expands to the wall. The plasma is then assumed to be wall confined, where heat loss is controlled by heat conduction across the fields inside the plasma. For a plasma of negligible resistivity and classical thermal conductivity, the rate of heat transfer to a cold wall is

$$q \approx 2.62 \times 10^{-21} \left[\frac{T^{3/2} n_i^3 \ln \Lambda}{B^2 t} \right]^{1/2} \text{ W/m}^2 \quad (4.1)$$

For typical post-burn parameters ($T = 20 \text{ keV}$, $n_i = 10^{20}/\text{m}^3$, $\ln \Lambda = 20$, and $B = 1 \text{ T}$), the heat loss to the wall is $1.1/t^{1/2} \text{ kw/m}^2$ which,

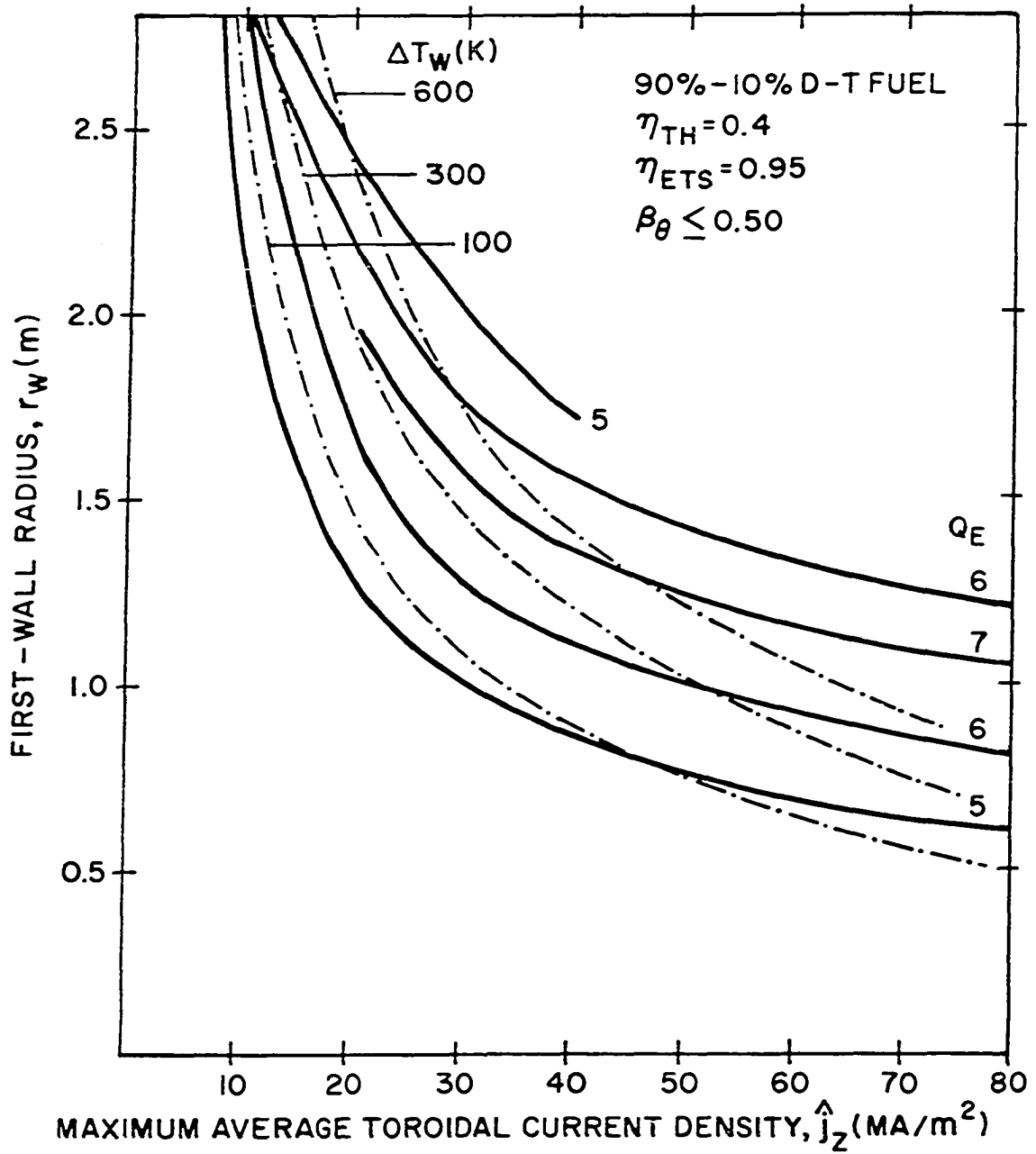


Fig. 10. Lines of constant Q_E for various first-wall radii r_w and maximum average toroidal current densities \hat{j}_z (solid curves) where a 90%-10% D-T fuel mixture is used. The dotted-dashed curves are lines of constant first-wall ((0.3 mm) Al_2O_3 /(5 mm) Nb-1Zr) surface temperature rise ΔT_w (K).

generally, is small compared to the radiation heat flux during the burn ($\sim 250 \text{ kw/m}^2$). The inclusion of a neutral gas between the plasma and the wall could prevent the wall from being damaged before the cool buffer layer is set-up within the plasma and could enhance the seemingly slow classical heat loss rate. For the tritium burnout case no energy is produced in the plasma during quench. In the 50%-50% D-T case no additional plasma energy is assumed by the energy balance to be added after plasma expansion to the wall, but a significant increase in Q_E may result because of additional alpha-heating power occurring during the quench phase.

The proposal of wall confinement at the end of the burn is preliminary, however, and must be studied in much greater detail. Of primary importance are transient effects which may determine the heat transport and surface damage to the first wall during the set-up phase of the wall-confined plasma.

D. Operating Point(s) Determination

Uncertainties in the plasma physics including plasma field profiles, resistivities, diffusion, achievable current densities, and stability makes the choice of any operating point for the RFPR questionable at this point. The two specific operating points shown below, therefore, are intended only to illustrate possible operating regimes.

An experimentally determined (12) value of the maximum achievable average toroidal current density is taken to be about 20 MA/m^2 . Using this constraint and imposing a reasonable limit on the first wall

temperature rise ($\Delta T_w (k) < 200$) leads to a reactor size of about 2 m for both cases. The time response of major variables is shown in Fig. 11 and Fig. 12, and reactor parameters and energies are given in Table 3.

An energy transfer and storage (ETS) system efficiency η_{ETS} of 0.95 was used in all the studies. The variation of Q_E versus η_{ETS} for the chosen reactor operating points is shown in Fig. 13. The characteristically efficient use of magnetic field energy by reversed-field pinches is reflected by the low values of η_{ETS} allowed for $Q_E = 1$.

For both cases the field annihilated inside the plasma W_B^{IN} constitutes ~50% of the total losses in the system. Hence, although the efficient use of magnetic field energy in a RFP configuration results in an energy balance which is less sensitive to η_{ETS} , this strong advantage is weakened somewhat by the need to provide for losses associated with trapped flux.

The startup for the two operating points proceeds as described in Sec. IV.A. A sinusoidal voltage of 10 kV/turn with a quarter period of 0.1 s appears virtually constant during the initial 0.012 s modeled by the tokamak startup code, or until T_E reaches 0.1 keV. The resultant plasma response is shown in Fig. 14. The initial rapid decrease in electric field to 6 V/m-mTorr involves the transition from the avalanche region ($n_e < 0.01 n_0$) with $T_e \sim 0.01$ keV to a Maxwellian electron distribution of lower temperature ($T_e = 0.003$ keV) where the high energy "tail" (energy above 0.015 keV) of the distribution ionizes the D-T

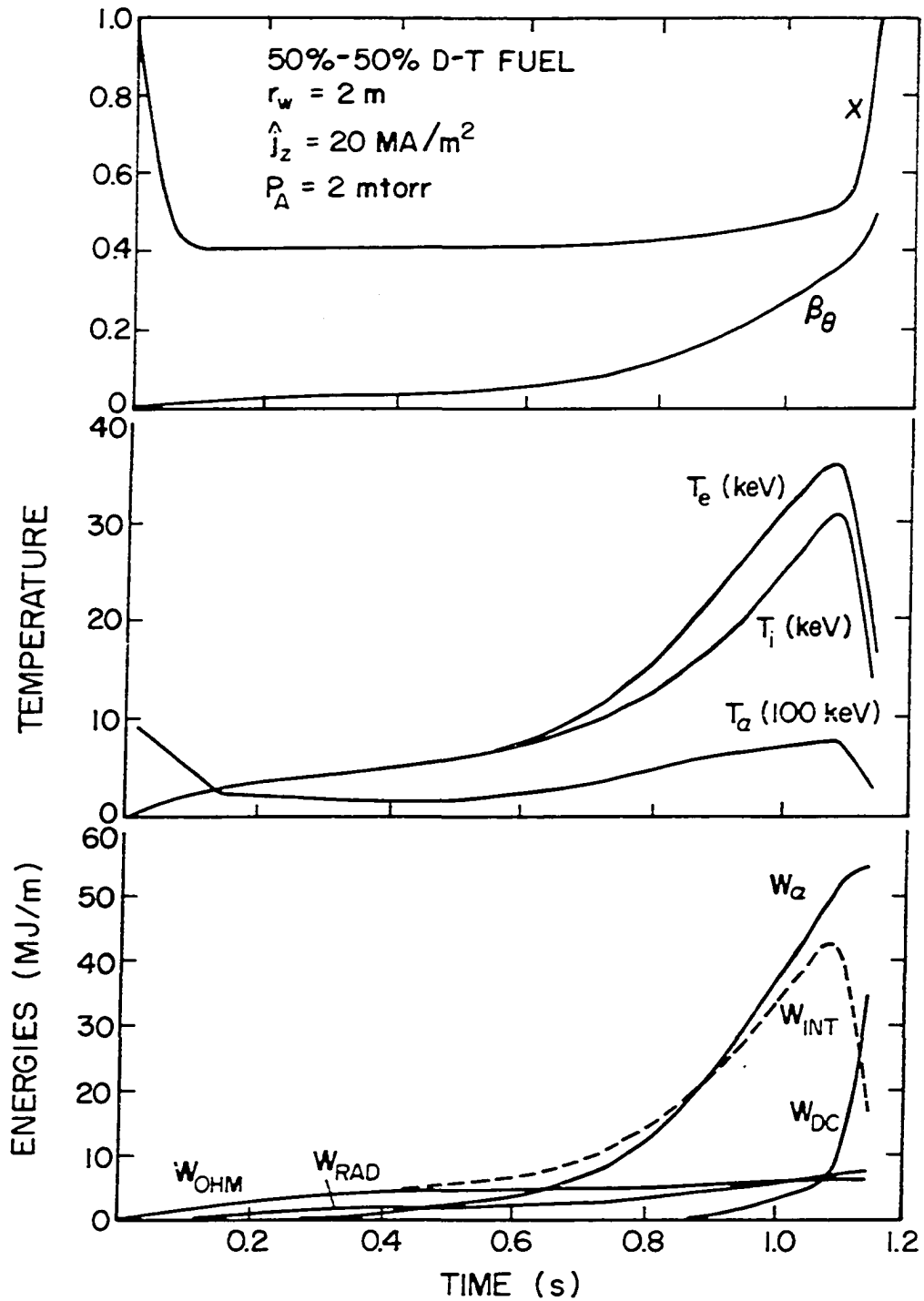


Fig. 11. Time-dependence of plasma and energy quantities for the 50%-50% D-T operating point summarized in Table 3.

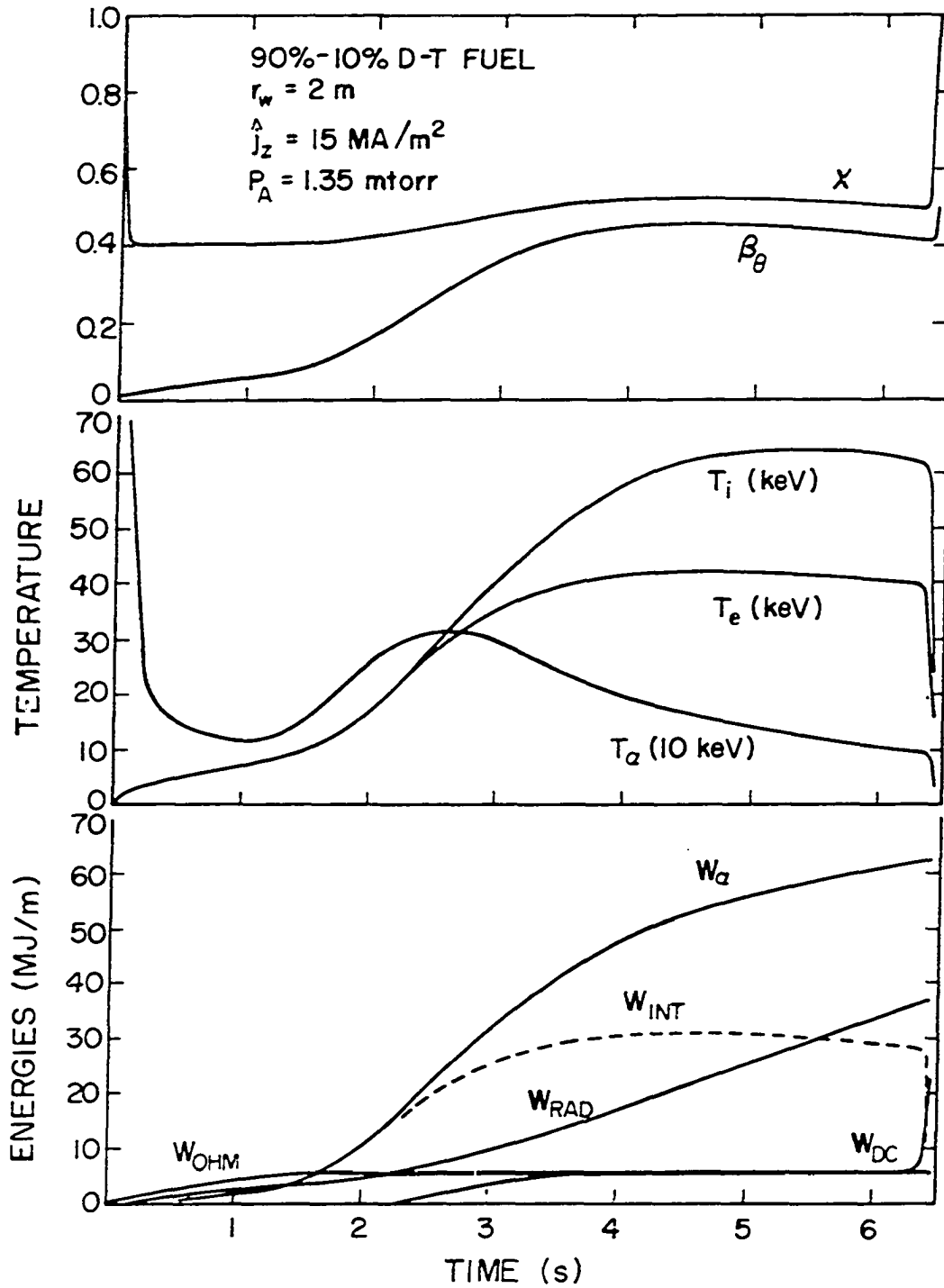


Fig. 12. Time-dependence of plasma and energy quantities for the 90%-10% D-T operating point summarized in Table 3.

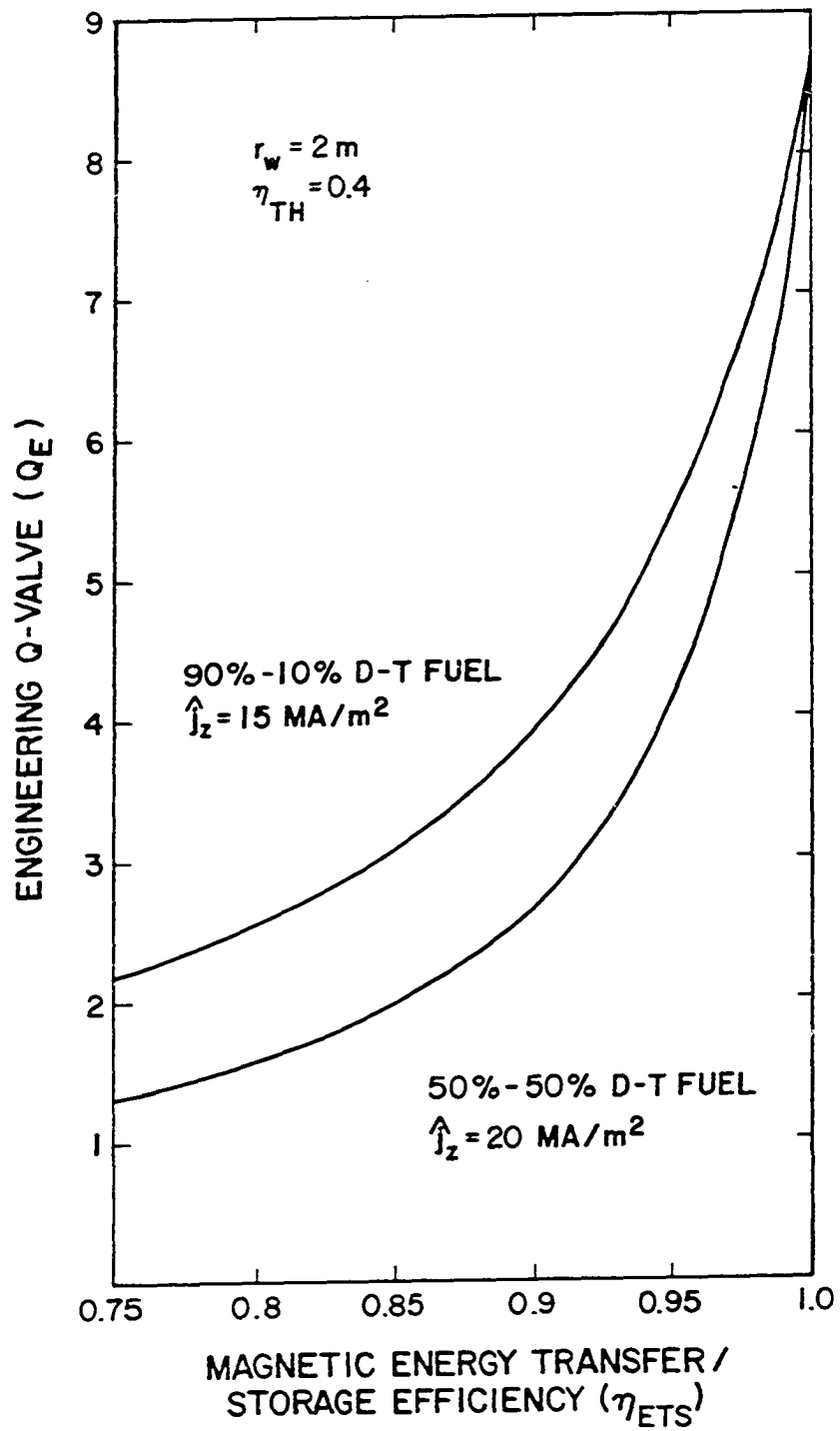


Fig. 13. Dependence of Q_E on the magnetic energy transfer/storage efficiency η_{ETS} for both cases investigated.

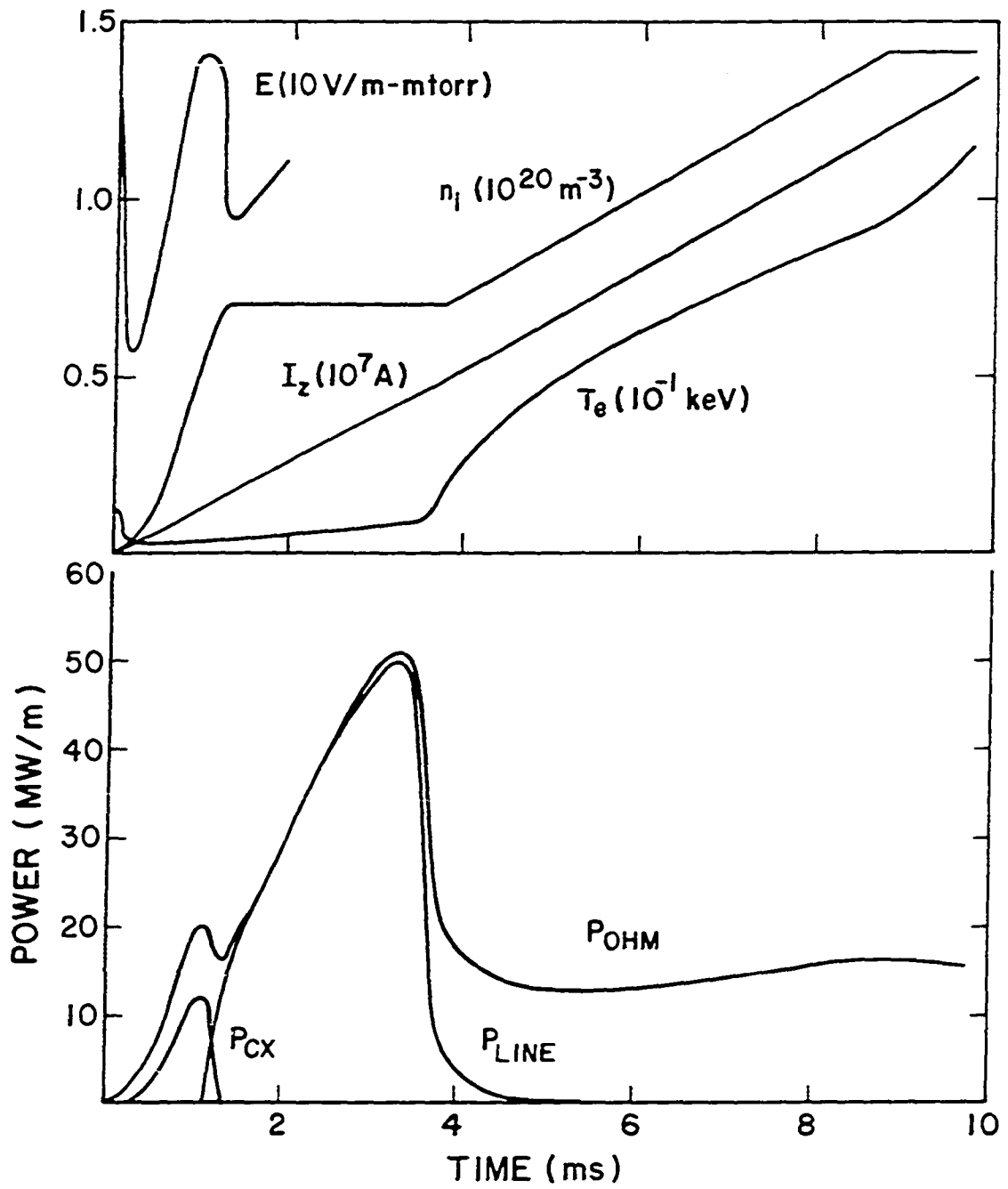


Fig. 14. Time-dependence of various plasma parameters and dominant powers for a tokamak-like RFPR startup.

Table 3. Summary of typical RFPR parameters

Symbol	Definition	50%-50% DT	90%-10% DT
r_w	first-wall radius (m)	2.0	2.0
x_m	minimum plasma compression	0.4	0.4
I_z	peak toroidal plasma current (MA)	40.0	30.0
\hat{j}_z	average toroidal current density at minimum compression (MA/m ²)	20.0	15.0
P_A	ambient D-T filling pressure (mTorr)	2.0	1.35
n_i	ion density at ignition (1/m ³)	8.52×10^{20}	5.82×10^{20}
$n\tau$	time-integrated Lawson parameter (s/m ³)	8.41×10^{20}	2.64×10^{21}
f_T	initial tritium atom fraction	0.5	0.1
f_B	fractional burnup	0.109	0.184
T_{if}	ion temperature prior to quench (keV)	14.4	23.8
T_{ef}	electron temperature prior to quench (keV)	16.3	15.3
$(dT/dt)_Q$	post-burn plasma reactivity (keV/s)	18.5	-0.41
W_{INT}^o	initial plasma energy (MJ/m)	0.086	0.058
W_{INT}	final plasma energy (MJ/m)	18.9	11.0
W_{BR}	bremsstrahlung energy (MJ/m)	5.38	19.9
W_{CY}	cyclotron energy into first wall (nonreflecting) (MJ/m)	1.72	16.9
W_N	fusion neutron energy (18 MeV/n) (MJ/m)	279.6	317.7
W_α	total-alpha particle energy (MJ/m)	54.7	62.1
W_{OHM}	plasma ohmic heating energy (MJ/m)	5.11	5.85
W_{COND}	thermal conduction energy (MJ/m)	0.036	0.24
W_{DC}	direct-conversion energy (MJ/m)	34.7	21.3
W_{BZ}	energy requirements of toroidal field system (MJ/m)	13.3	7.3

Table 3 (Continued)

Symbol	Definition	50%-50% DT	90%-10% DT
W_{BP}	energy requirements of poloidal field system (MJ/m)	345.4	205.0
W_{BO}	total magnetic energy in ETS system (MJ/m)	358.7	212.3
W_{TR}	transport losses in coil and leads (MJ/m)	6.23	11.5
W_{ED}	eddy current losses in coil, leads, and blanket (MJ/m)	0.67	0.79
W_B^{IN}	field in plasma at end of burn (MJ/m)	37.1	19.6
W_{ETS}	ETS transfer losses ($1 - \eta_{ETS}$) W_{BO} (MJ/m), $\eta_{ETS} = 0.95$	17.9	10.6
W_{TH}	total recoverable thermal energy (MJ/m)	342.7	385.5
W_{ET}	gross electric energy $\eta_{TH} W_{TH}$ (MJ/m), $\eta_{TH} = 0.4$	137.1	154.2
Q_E	engineering Q-value	4.06	5.39
W_C	total circulating energy (MJ/m)	33.8	28.6
ϵ	recirculating power fraction $1/Q_E$	0.25	0.19
W_E	net electric energy ($1 - \epsilon$) W_{ET} (MJ/m)	103.3	125.6
η_p	overall plant efficiency $\eta_{TH}(1 - \epsilon)$, $\eta_{TH} = 0.4$	0.30	0.33
R	major radius (m)	10.0	10.0
τ_C	cycle time (s)	8.65	10.5
τ_B	burn time (s)	1.14	6.44
I_w	14 MeV neutron wall loading (MW/m ²)	2.00	1.87
P_{TH}	total thermal power (MWt)	2490.	2300.
P_{ET}	system gross electric power (MWe)	995.	921.
P_C	system circulating electric power (MWe)	245.	171.
P_E	net system electric power (MWe)	750.	750.

neutrals. The electric field on the plasma then varies between 6-14 V/m-mTorr as the bulk of the neutrals are ionized.

The major power contributions are also shown in Fig. 14. The difference between the ohmic-heating power P_{OHM} and ion-neutral charge-exchange power P_{CX} is the power required to ionize the D-T neutrals. The large line radiation power P_{LINE} at 0.01 keV is apparent where a 1% oxygen fraction is assumed. After the resonance line is overcome ($T > 0.02$ keV), the initial density corresponding to 1 mTorr is increased to 2 mTorr in 0.005 s for the 50%-50% D-T case while holding the impurity fraction constant. The bremsstrahlung power during this early phase increases to a maximum of only 0.3 MW/m at 0.012 s, and the cyclotron radiation is insignificant. The ion and electron diffusive energy loss terms are less than 0.01 MW/m.

The impurity fraction used above for illustrative purposes during startup was taken to be zero during the burn to reduce the parameter space. The initial starting density may be reduced until electron runaway becomes serious. The initial inductive spike begins at ~ 75 V/m-mTorr and drops to 20 V/m-mTorr after 15 μ s for 1 mTorr. As the density is decreased the initial large electric field is maintained for longer periods of time and, for ionization below 10%, continues to increase until large numbers of electrons runaway and the discharge fails to develop. An experimentally determined filling pressure of 0.1-0.2 mTorr (46) for a radius of ~ 0.5 m gives an estimate of the minimum value. The startup code predicts an electric field > 20 V/m-mTorr during the period when $n_e < 0.1 n_o$ at these minimum

densities. Changing the applied voltage on the system proportionally varies the time scale, however the magnitude of all quantities plotted in Fig. 14 remain virtually unchanged. Doubling the voltage would then decrease the time scale by one-half.

V. FINAL SYSTEM DESIGN

A. General Reactor Description

The toroidal reversed-field pinch reactor investigated here is a pulsed-plasma device using a lithium-sodium-steam heat transport system with a thermal cycle efficiency of 40% to produce 750 MWe at an overall plant efficiency of 30-33%. The major reactor parameters are listed in Table 3 for the two chosen operating points. The design given herein is based primarily on the 50%-50% D-T fuel mixture case although both cases are similar. A plan view of the reactor system containing key RFPR subsystems is given in Fig. 15. The details of the heat removal and thermal conversion systems are described in Reference 73 for the Reference Theta Pinch Reactor. Two coolant loops of ~1250 MWt each transport the heat from the reactor to the single turbine/generator set. The schematic diagram of the primary-coolant circuit in Fig. 16 illustrates the major lithium flow paths. The primary lithium coolant removes heat from the reactor blanket (lines denoted 1-7 in Fig. 16) and provides the tritium breeding necessary for the deuterium-tritium fusion burn cycle. Because of the cyclic nature of the plasma fusion, the lithium flow is reduced to near zero when magnetic field is present in the reactor blanket. During this period of the burn cycle the lithium flow must be shunted to an upstream surge tank while a downstream surge tank continues to flow lithium to the intermediate heat exchanger. When the magnetic field is zero, the lithium flows through the blanket, and the upstream tank empties while the downstream tank refills. The

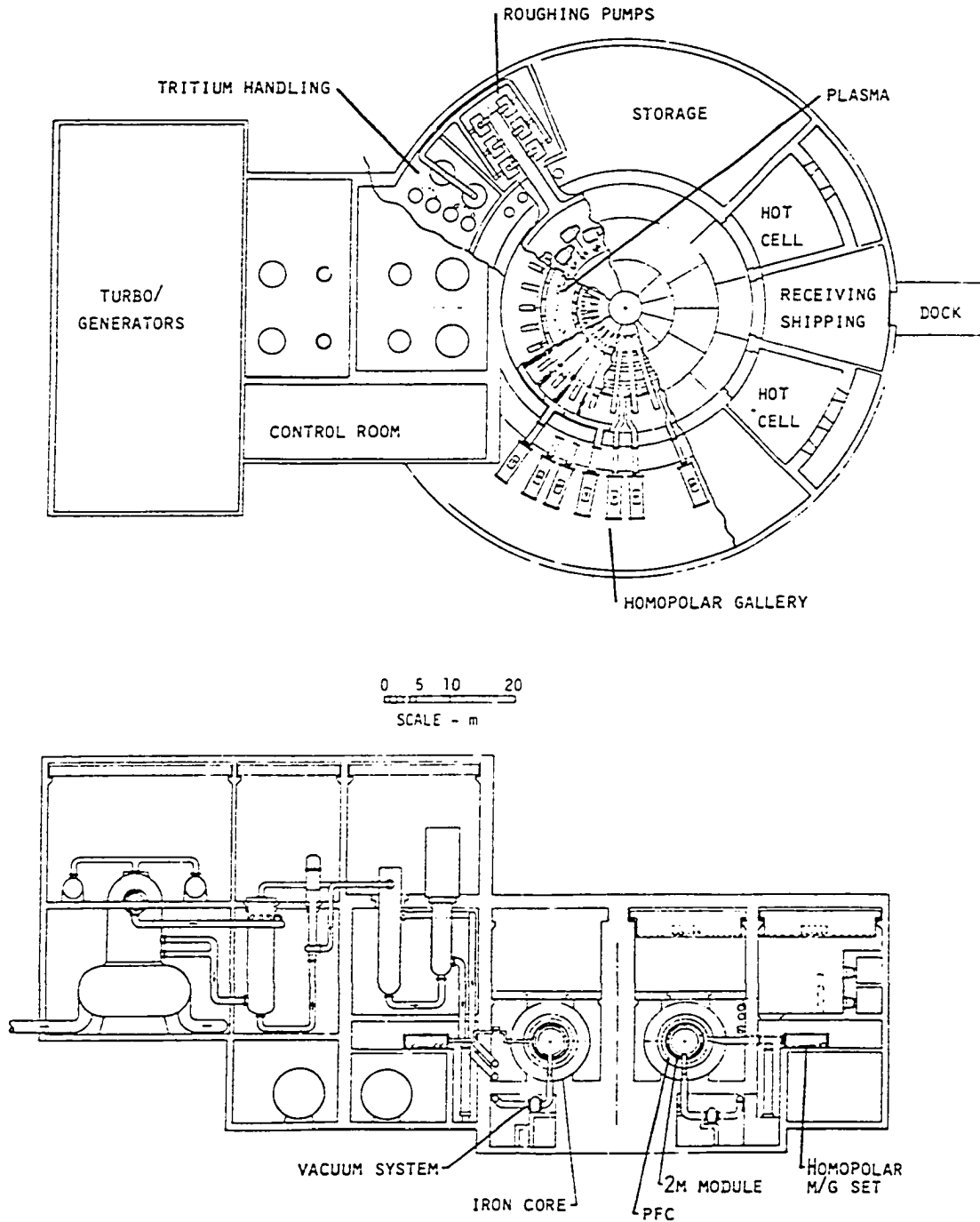


Fig. 15. Plan and elevation view of 750 MWe (net) RFPR.

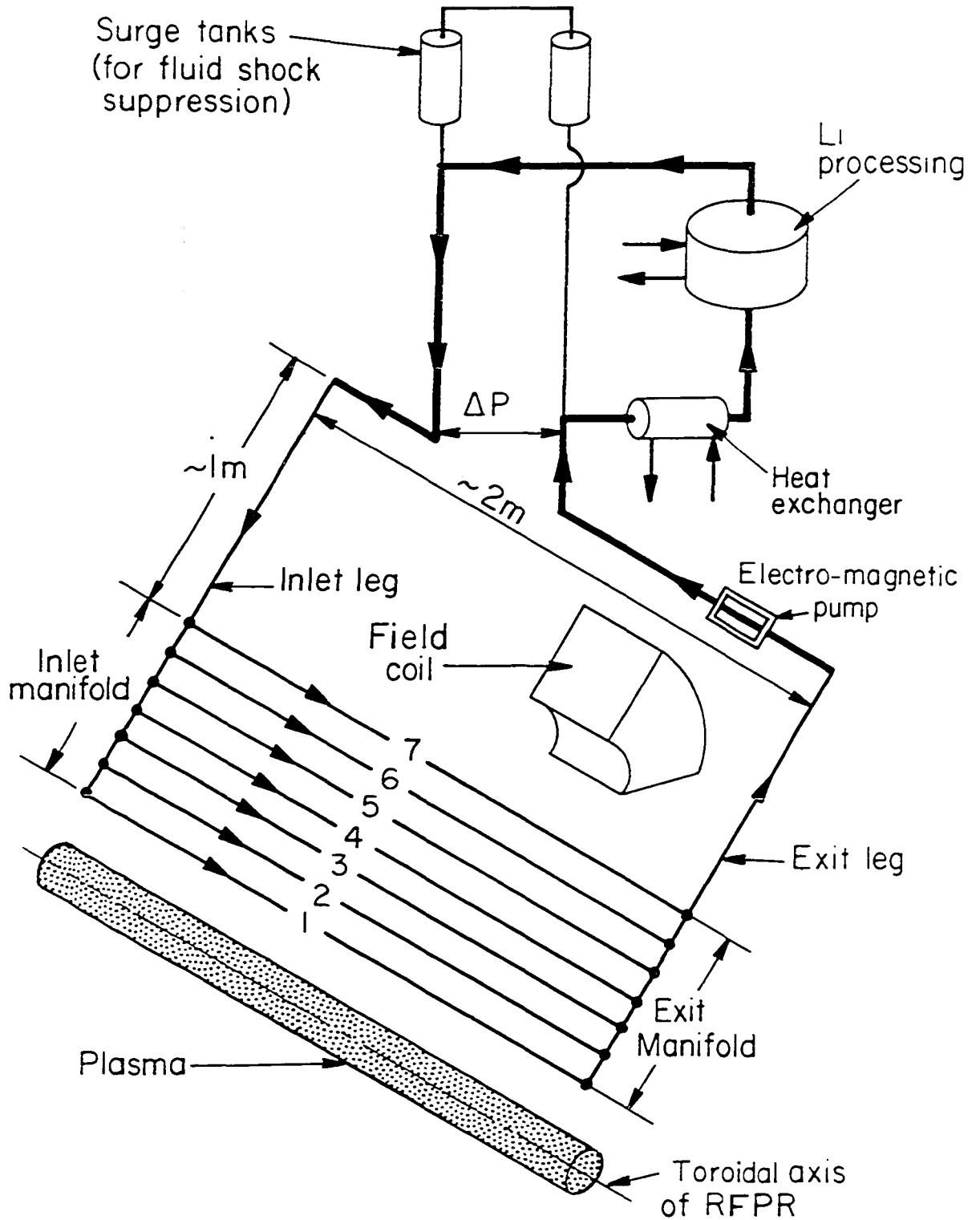


Fig. 16. Schematic diagram of the primary-coolant circuit illustrating the major lithium flow paths.

lithium which flows from the heat exchanger is purified and the tritium extracted (73).

A lithium exit temperature of 820 K produces a sodium exit temperature of 810 K from the Li-Na heat exchangers. The remainder of the plant is then similar to the Liquid-Metal Fast-Breeder Reactor designs. The plant operates at 755 K maximum steam temperature which is similar to the design temperatures of many fossil-fuel plants presently in operation. An overall thermal cycle efficiency of $\eta_{TH} = 0.40$ results and is used for all calculations.

As shown in Fig. 15, the reactor is comprised of 30, 2.1-m-long toroidal sections resulting in a torus of 10-m major radius. An isometric view of a RFPR segment, given in Fig. 17, shows the placement of major reactor components. The first wall also acts as the vacuum wall where the flanges at the ends of the 2.1-m modules are welded to form a vacuum seal. The lithium-cooled blanket, and toroidal field coil (TFC) is then encircled by a structural ring which is used to lift the 2.1-m module. The blanket/first-wall assembly and vacuum ducting for each module is mechanically separate and supported by the iron core structure. Outside of the modules are the poloidal field coils, divided into 4-m-long toroidal sections, and the iron cores, divided into top and bottom semicircular sections. The actual amount of iron necessary to reduce the externally stored energy to near zero is much more than shown in Figs. 15 and 17 and is discussed in Sec. V.B.

Referring to Fig. 17 a vacuum pump and associated ducting is provided for each 2.1-m-long module with the vacuum tunnel underneath

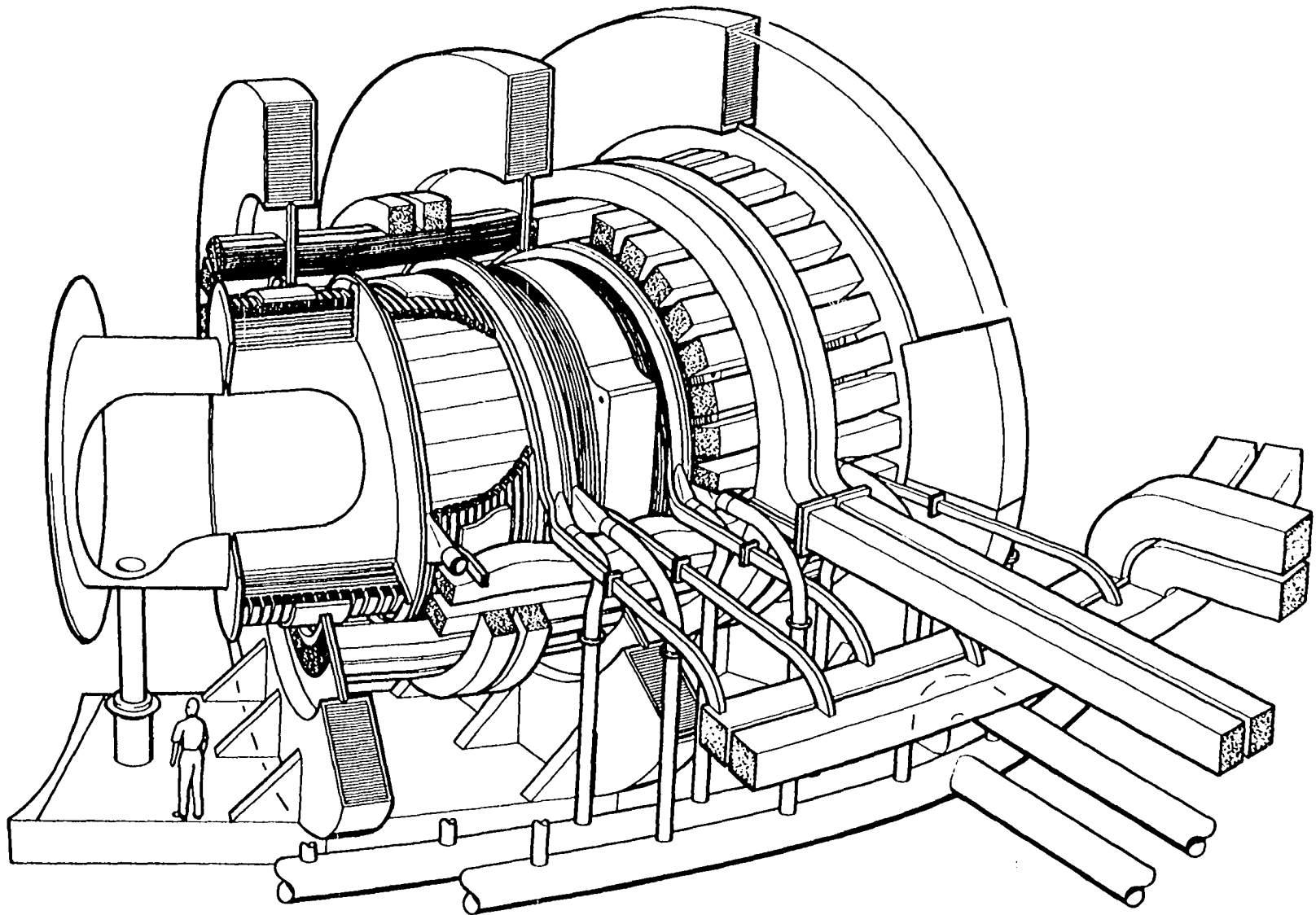


Fig. 17. Isometric view of 2-m-long RFPR reactor modules (vacuum vessel, blanket, toroidal field coil) and associated poloidal field coil assembly and iron-core pieces.

the floor of the reactor. The inlet and outlet lithium coolant pipes encircle the torus at the reactor floor level and separate connections are made to each module. The TFC's are connected electrically in parallel to a bus which also encircles the machine and is energized by two center-grounded homopolar machines. The poloidal field coil (PFC) consists of wedge-shaped segments where 1/15 of the conductors in each wedge are energized at each 4-m-long section, resulting in a single turn transformer coil when the 15 sections are connected. Each of the PFC leads is then connected to two center-grounded homopolar machines.

The plant layout given in Fig. 15 depicts the general scheme envisaged for repair and maintenance of the RFPR. All major operations on the reactor torus must be made remotely with the aid of a ~200-Tonne-capacity overhead crane. Access to a given 2-m-long x 5.5-m diameter x 100-Tonne module is achieved after removal of the overhead shielding blocks, the top halves of three adjacent iron-core pieces, and the top half of the associated 4-m-long x 175-Tonne PFC assembly after disconnecting the electrical leads and associated coil (He-gas) coolant leads. The bottom halves of both iron-core pieces and PFC assembly need not be removed to replace a RFPR module. Disconnection of TFC leads and associated coolant lines, and remote grinding of welded vacuum joints between the adjacent modules as well as joints connecting the module to the vacuum downcomer allows the module under repair to be removed from the torus and placed in an appropriate repair or salvage area.

The 20-30 homopolar generators used to energize the coils would be mounted on rails and could easily be decoupled from the massive but permanent lead structure. A similar arrangement is envisaged for the banks of vacuum pumps with the additional difficulty of remote maintenance due to the intense neutron bombardment of the vacuum system. The technology associated with the large number of remote manipulations of massive equipment will require considerable development. Other required reactor subsystems such as tritium handling/processing, He-gas coolant system for the coils, cryogenic facility for the superconducting homopolar energy stores, plant control system, and associated maintenance machinery have not been investigated and must be addressed in future RFPR design studies. The balance of plant appears "standard" except for the Na/Li primary heat exchangers and Li pumps.

B. Consideration of Major System Components

The major components to be described are the fuel supply and removal system, first wall and blanket, magnet coils, iron core, homopolar energy storage devices, and switches. This design has not progressed into the detailed engineering stage, and specific structural analysis of these subsystems is not addressed.

The fuel supply and removal system must provide a DT mixture at the pressure required for the plasma burn phase ($\sim 1-2$ mtorr), supply a sufficient amount of neutral gas (DT mixture) to quench the plasma, and reduce the concentrations of reaction products (helium) and other impurities between plasma burn pulses. The fuel supply will use

straight-forward gas-puff methods through small tubes (~ 1 mm) at a few locations around the torus providing ~ 1600 l-Torr (~ 0.6 g T) fuel charge (2 mTorr) for a burn pulse and an additional amount for the plasma quench. Given that each 25 m^3 module is equipped with a vacuum "downcomer" which represents the minimum vacuum conductance, the maximum pumping speed is then determined by this conductance. Under the anticipated condition of molecular flow, the downcomer conductance is given by (74)

$$C = \frac{651 \pi a^2}{1 + \frac{3}{8} \frac{l}{a}} \text{ m}^3/\text{s} \quad (5.1)$$

where a is the duct radius taken as 0.2 m and the length l is 1 m, resulting in a $28.5 \text{ m}^3/\text{s}$ conductance. Dividing the conductance into the module volume yields an e-folding time of ~ 0.9 s, and a few seconds of pumping through this conductance will reduce the concentration by ten. This ideal situation does not account for the added gas load which may be incurred by the as yet unresolved requirements of the quench and plasma cooling phases of the burn cycle. A Roots blower (with associated roughing pumps) is envisaged for the primary pumping system and when impedanced matched with a 25,000 l/s conductance would be ~ 1.6 m diameter x 3.6-m-long and consume 100 kWe/module (73).

The lithium-cooled (99% enriched ^7Li), Nb-1Zr blanket system is described in References 15 and 75 and is shown schematically in Fig. 18. The 0.4-m-thick blanket with 1 to 2-mm-thick niobium structural walls uses stagnant lead for neutron multiplication in the hard-spectrum regions, stagnant ^6Li (95% enriched) for tritium production leading to

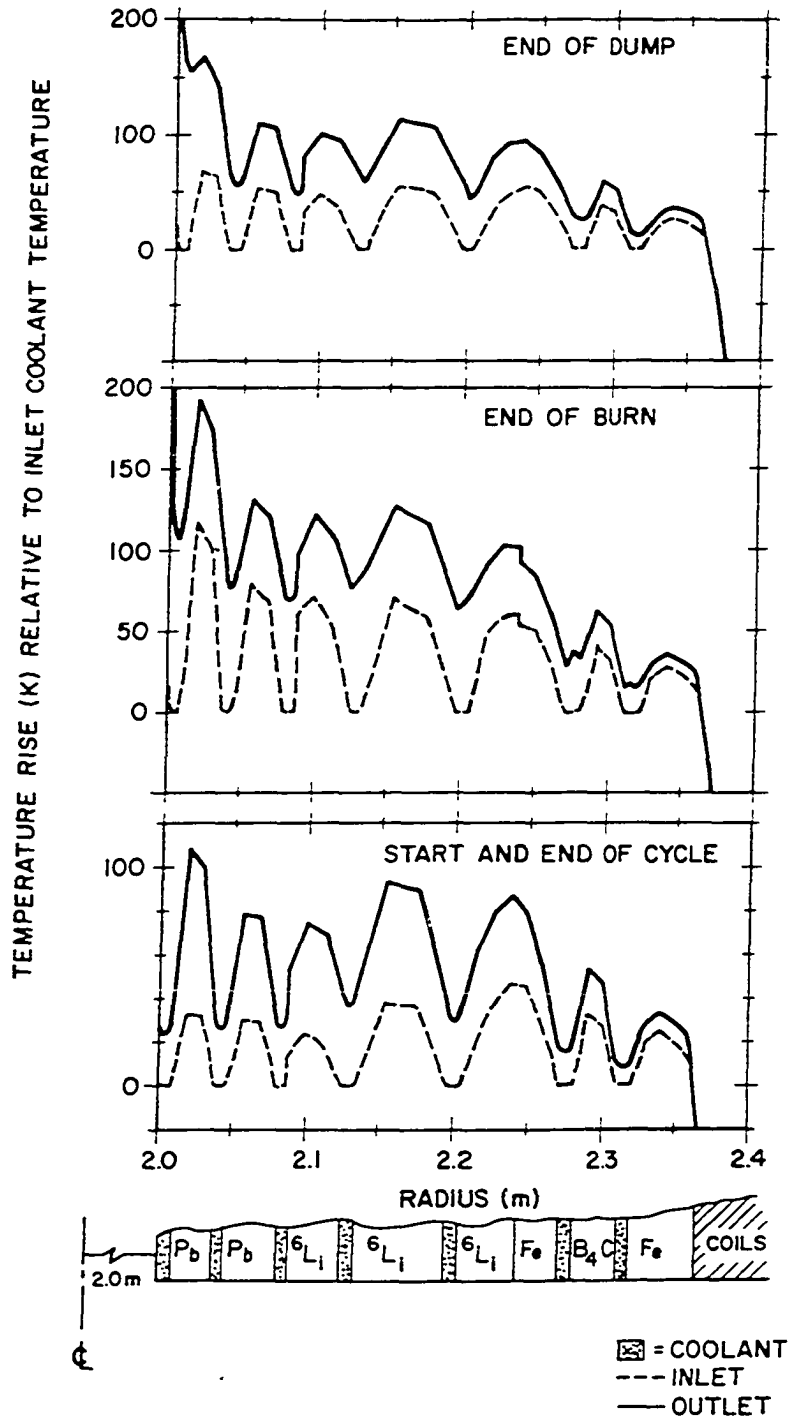


Fig. 18. Time dependence of the blanket temperature distribution for the 50%-50% D-T burn cycle summarized in Table 3.

an overall tritium breeding ratio of 1.10, and a combination of iron and boron carbide for attenuation of gamma rays and slow neutrons. Efficiency of the blanket in capturing neutron energy is to be near 100% resulting in a total thermal energy of 18 MeV/neutron. Division of the blanket into 30 azimuthal sections (Fig. 17) reduces the eddy-current losses.

The coolant-flow response shown in Fig. 19 and resultant temperature profile shown in Fig. 18 use parameters from the 50%-50% D-T fuel mixture case where the numbered coolant flow curves correspond to the flow channels in the blanket also shown schematically in Fig. 16. During the burn (when magnetic field is present) the lithium flow is very small, and the heat transfer to the coolant is primarily by conduction. During the quench phase (plasma dump) the net plasma current is electrically forced to zero resulting in a wall-confined plasma with no field outside the reacting volume which allows the coolant to flow.

The required image currents for plasma stability (see Sec. II.A) are assumed to be provided by the first wall and blanket on short time scales ($\tau \sim \delta^2 / (0.5 \times 10^6 \eta)$ where $\eta = 2 \times 10^{-6} \Omega\text{-m}$ for 1000 K Li gives $\tau \sim 0.1$ s for the $\delta \sim 0.4\text{-m}$ -thick blanket) and external windings for longer times. This is speculative and further investigation may lead to the inclusion of a low resistivity material near the first wall. A prime candidate would be copper near room temperature which would require a blanket that thermally isolated a cool copper region (immediately outside the first wall at 800-1000 K) from the remainder of

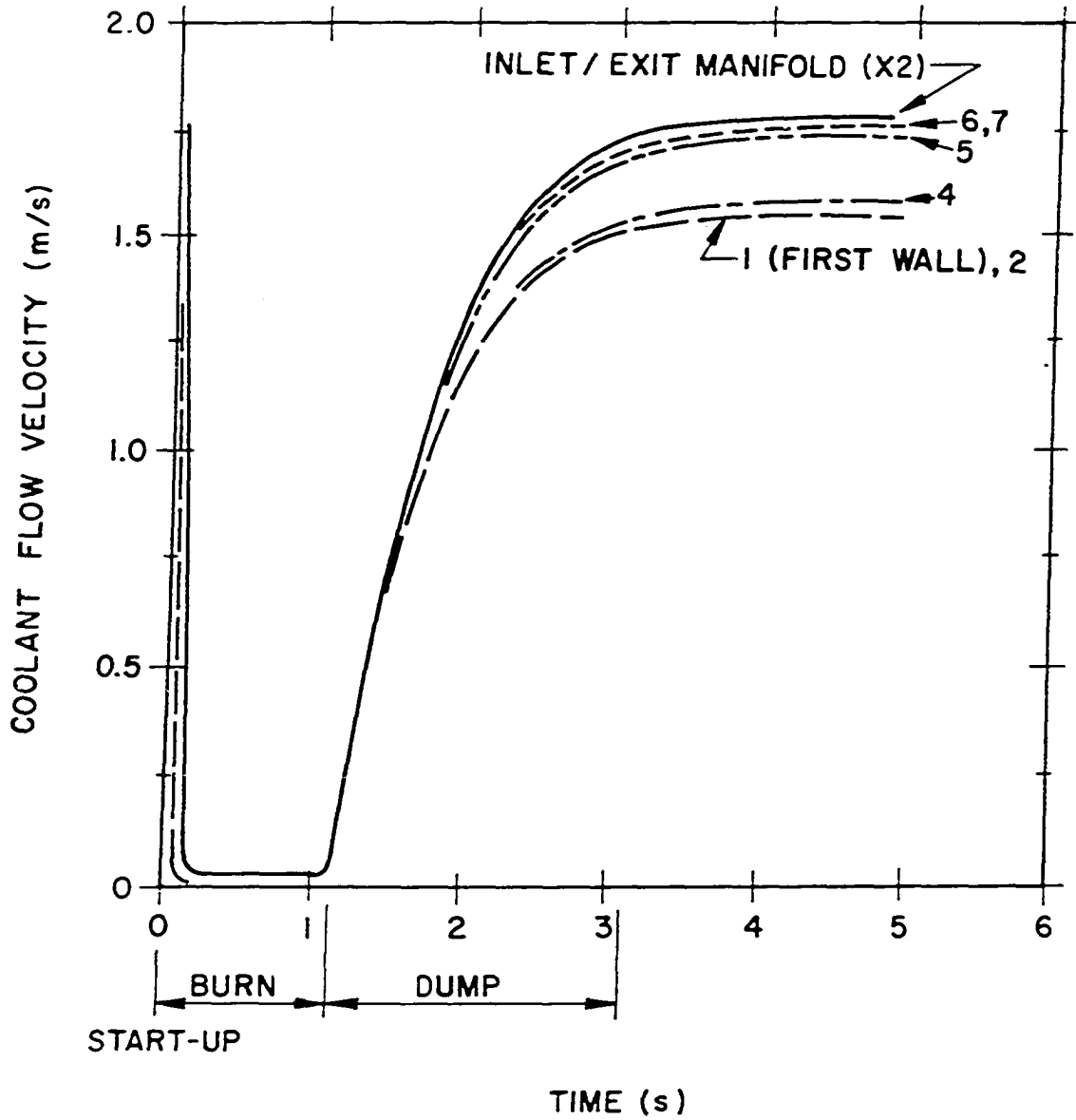


Fig. 19. Time dependence of lithium coolant flow in the RFPR blanket for the 50%-50% D-T fuel mixture case.

the blanket. The additional energy loss and complexity of this system is much less favorable than the blanket used in this design.

A first wall consisting of a low-z ceramic coating bonded to a structural metal is used as the reference design. For both cases given in Sec. IV, a (0.3 mm) Al_2O_3 /(1.0 mm) Nb-1Zr laminated wall is found to be adequate. A one-dimension heat transfer calculation in cylindrical geometry is performed vs time by the plasma burn code for the composite wall using the aforementioned lithium flow rates. Thermophysical properties are taken from Ref. 14. Tangential stresses for a composite cylinder under plane-strain conditions (14) are simultaneously calculated vs time and radial position using the temperature profiles. For all calculations the bremsstrahlung, cyclotron, and thermal conduction is taken as a surface heat flux, while the neutron-gamma heating (73) is assumed uniform. Figures 20 and 21 give the time dependence of temperature and tangential stresses at key locations within the first wall for the 50%-50% D-T case and 90%-10% D-T case, respectively. The 50%-50% D-T case has a 1.14 s burn followed by a quench phase when the trapped field W_B^{IN} and plasma internal energy is uniformly deposited at the first wall over a time period of 3 s. The lithium coolant starts to flow after the thermonuclear burn is complete. The 90%-10% D-T case shown in Fig. 21 has a 6.44 s burn and a 2 s quench phase. The ultimate compressive and tensile strength of Al_2O_3 is -7×10^8 Pa and 1.6×10^8 Pa, respectively. The stresses in the alumina are mostly compressive and a factor of at least three less than the ultimate stress. The first-wall composite has been experimentally (76) cycled in excess of a hundred

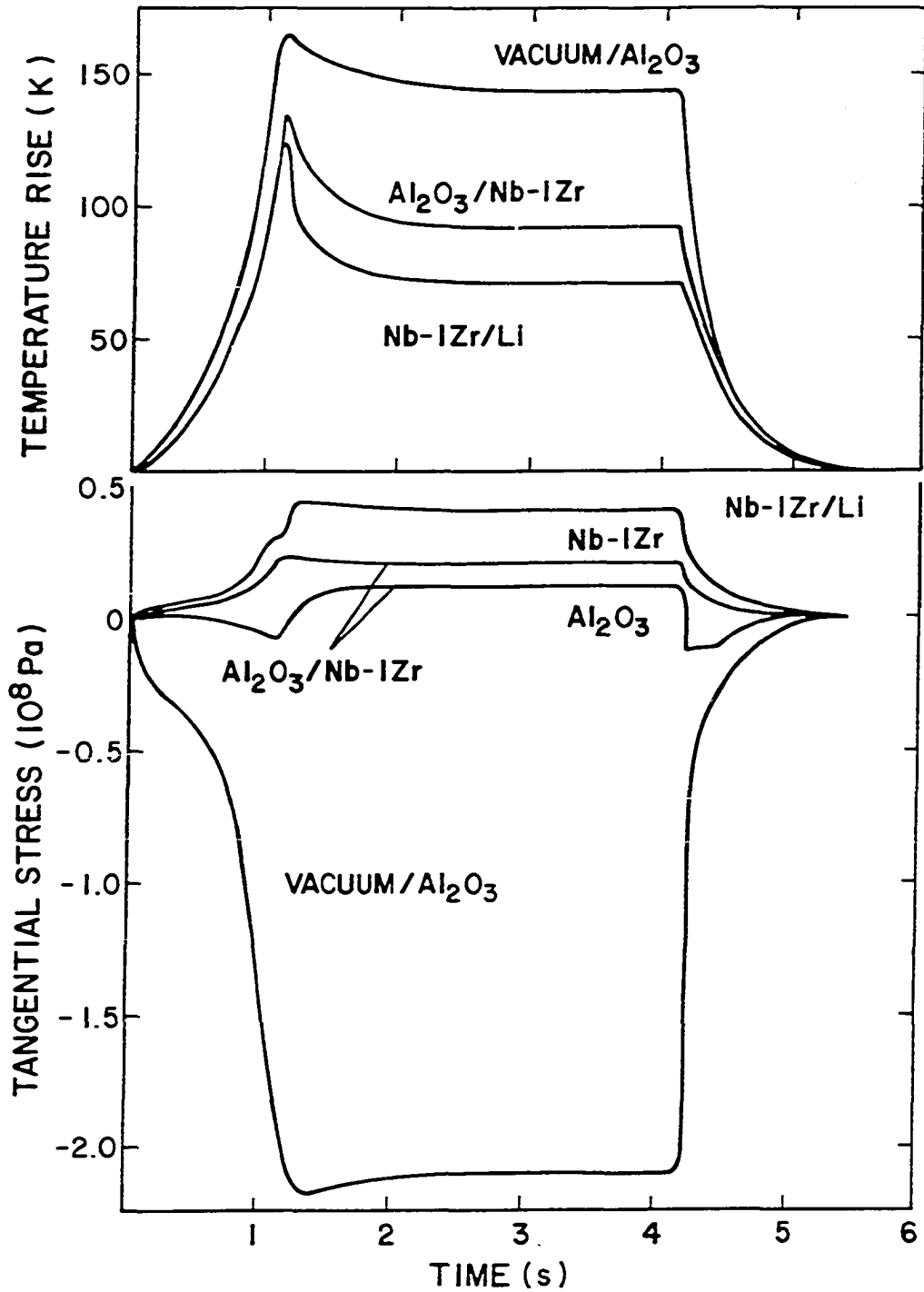


Fig. 20. Dependence of first-wall temperature and stress during the ignition, burn, quench, and plasma cooling periods associated with the 50%-50% D-T burn cycle given in Table 3.

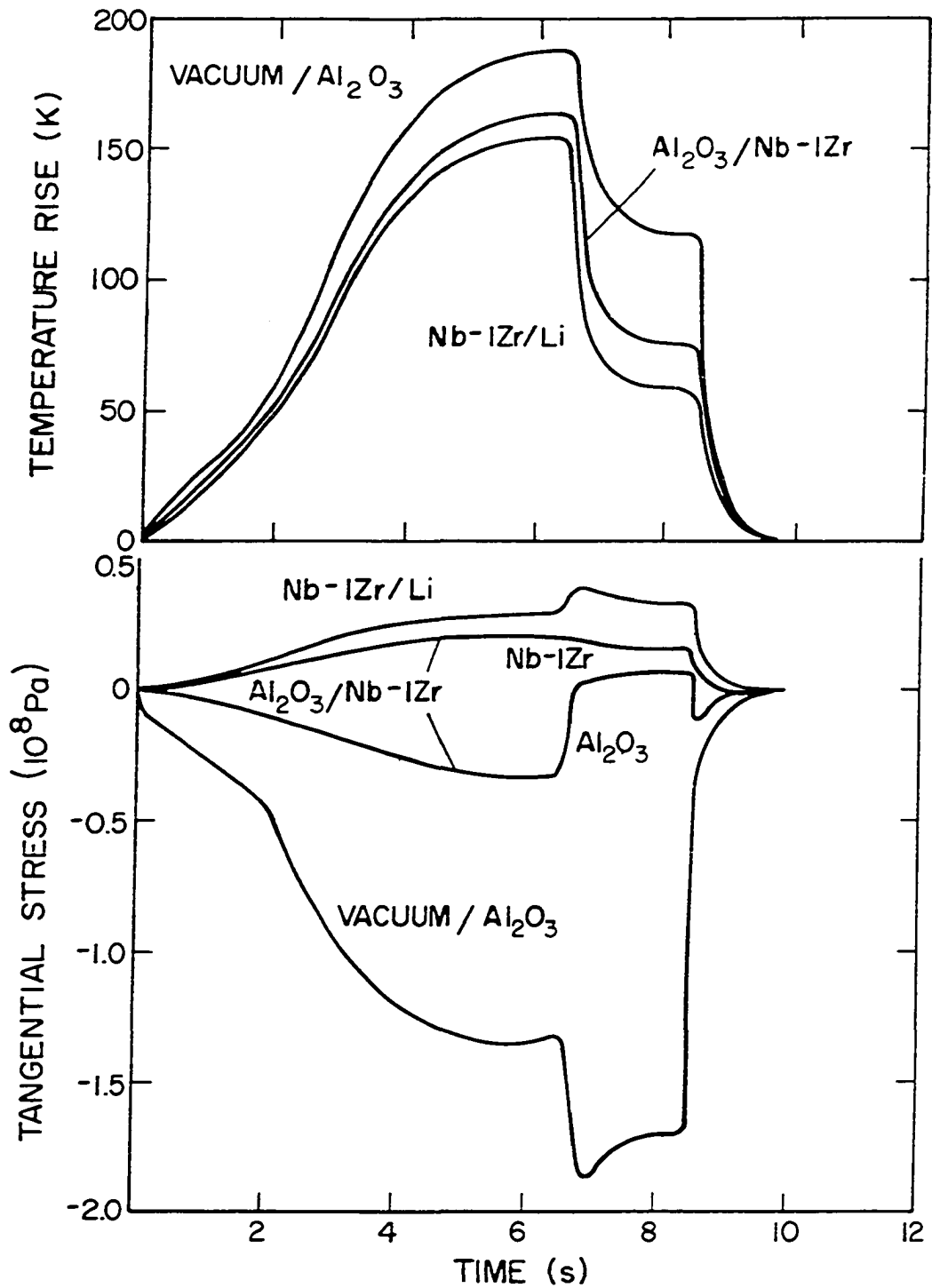


Fig. 21. Dependence of first-wall temperature and stress during the ignition, burn, quench, and plasma cooling periods associated with the 90%-10% D-T burn cycle given in Table 3.

times using a surface heat flux (pulsed electron beam). The resultant temperature excursions produced compressive stresses (computer simulation) at the alumina surface of -6×10^8 Pa and tensile stresses of 1.4×10^8 Pa in the alumina at the $\text{Al}_2\text{O}_3/\text{Nb-1Zr}$ interface. The actual stresses experienced by the RFPR first wall are well below these experimental values and appear to provide a reasonable margin of safety. The lifetime of the Nb-1Zr structural material is determined by thermal fatigue considerations. The maximum stress occurring in the Nb-1Zr is three times less than the yield strength of the material (1.4×10^8 Pa) at the operating temperature which should provide an adequate engineering safety factor, however, radiation damage is not considered.

The elements of the electrical system include a number of homopolar machines, switches, the toroidal/poloidal field coils and an iron core arranged in a toroidal configuration. The electrical circuit is a basic LC or tank circuit wherein the homopolar machine acts as a capacitor. The current/field relationships vs time are shown in Fig. 22. The poloidal and toroidal field systems are electrically separate (although inductive coupling will occur).

Opening and closing of switch S_1 is in effect performed by the homopolar brushes. Closure of switch S_1 (i.e., lowering the brushes) at time $-\tau_R/2$ connects the homopolar machine (100% speed and voltage) to the toroidal field coil. The current rises to a maximum producing the initial bias field B_{z0} . Preionization of the plasma now occurs and the analogous switch S_1 on the poloidal field system is closed. The current I_2 rises to a maximum as the B_z field continues to inductively "ring",

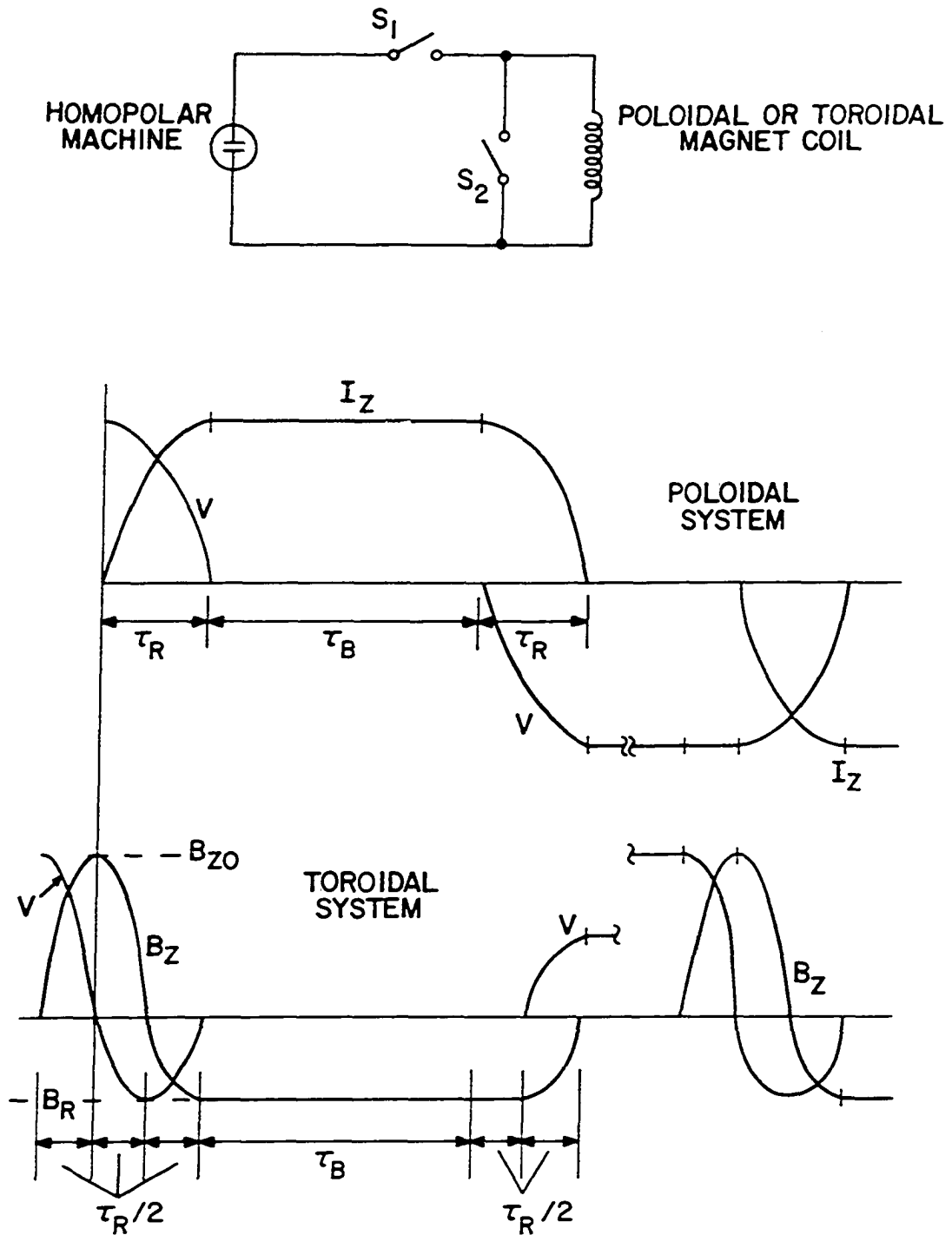


Fig. 22. Schematic diagram of homopolar-generator driven circuit for both TFC and PFC systems. The voltage $V \sim 4-5$ kV, the rise time $\tau_R \sim 100$ ms, and $\tau_B \sim 1-6$ s.

ultimately yielding the desired reversed field $-B_R$. At time τ_R switch S_2 is closed and the current I_z and reverse field $-B_R$ is maintained at a near constant value during the burn τ_B . The homopolar machine remains at rest during the period τ_B .

Following the burn, the switch S_2 is opened and the respective currents for each system are transferred back to the homopolar machine which motors up to 100% speed and voltage (neglecting losses). The above cycle is then repeated at the desired rate. The direction of rotation and the voltage of the homopolar machine in the poloidal system reverses during each cycle. If this results in stability problems, the field may be maintained in a uniform direction by the introduction of reversing switches.

The toroidal field coil, located immediately outside the blanket (Fig. 17), consists of 30 separate coils of 15 turns each (corresponding to a 2.1-m module) arranged electrically in parallel resulting in a voltage comparable to that of the poloidal system. The single-toroidal bus is then driven by two homopolar machines acting in series which are center grounded to minimize the machine voltage above the ground potential. The single-turn poloidal field coil is divided into 30-wedge-shaped segments (Fig. 17) in the azimuthal direction. These coils are then further divided into 4-m-long sections fed by a single electrical lead where 1/15 of the conductors in each wedge are energized at each lead resulting in a single-turn transformer coil when the 15 sections are connected. The upper and lower hemisphere of 4-m-long conductor is constructed as a unit with a single lead disconnect. Each

poloidal field is driven by two center-grounded homopolar machines. The poloidal field coil wedges and each turn of the toroidal field coil are contained within a stainless steel vessel providing a coolant path for the helium gas which maintains the coils at near room temperature to minimize ohmic losses. These coils would be constructed from ~ 7 mm copper bars that are litzed and transposed to produce a uniform current density in the magnet coils.

An equivalent circuit for the poloidal field system is the parallel connection of a capacitor (homopolar generator) and the inductors L_i and L_e associated with the regions internal and external to the poloidal field coil, respectively. The internal inductance is

$$L_i = \mu_0 R \left[0.5 + \ln \frac{r_{cp}}{r_p} \right] \text{ H} , \quad (5.2)$$

while the external inductance is

$$L_e = \mu_0 R \left[\ln \frac{8R}{r_{cp}} - 2 \right] \text{ H} \quad (5.3)$$

for an air core, and is considered to be infinite for an iron core. Thus, the iron core ideally couples the current in the poloidal coil (I_c) to the plasma current ($I_c = I_z$) and requires a total stored energy in the homopolar generators of

$$W_{\text{IRON}} = 0.5 L_i I_z^2 . \quad (5.4)$$

For an air core the current swing in the poloidal field coil is $L_e \Delta I_c = (L_e + L_i) I_z$ (equating flux change) which yields $\Delta I_c = 97.5 \text{ MA}$ for the

50%-50% D-T case in Table 3 ($I_z = 40$ MA, $L_e = 1.6 \times 10^{-5}$ H, and $L_i = 2.3 \times 10^{-5}$ H). Swinging the current in the coil from 0 to 97.5 MA increases the ohmic losses a factor of 6 ($\propto I_c^2$) and requires a total stored energy of

$$W_{AIR} = 0.5 L_e (I_c - I_z)^2 + 0.5 L_i I_z^2 \quad (5.5)$$

(evaluated at maximum I_z) or nearly 2.5 times the iron core case. By swinging the primary coil current from -48.75 MA to +48.75 MA the ohmic losses are only 1.5 times and the stored energy required nearly equal to the iron core case. This appears favorable, however, the extraction of the field energy from the poloidal coil at the end of the burn is exceedingly difficult. The coil current is swung from plus to minus 48.75 MA which drives the plasma current to zero. If the external circuit now attempts to drive the coil current to zero, the flux change induces a current in the hot conducting plasma which implies that the coil current cannot be extracted until after the quench (2-3 s). In this case the current should simply be left in the coil; using the homopolar generator as a transfer capacitor to symmetrically swing the current from plus to minus now only requires an energy store equal to half that needed by the iron core case. Operating in this mode greatly increases the ohmic losses in the coil when compared to an iron core system.

An iron core is assumed herein for all cases, which reduces the coil ohmic losses and required stored energy (maximizes Q_E) when compared to an air core system (excluding minus to plus poloidal current swings due

to the aforementioned field energy extraction problems). The cross sectional area, A , of iron required is

$$2B_s A = L_p I_z \quad \text{Wb} , \quad (5.6)$$

where B_s is the saturation flux taken as 2 T, and the factor of two accounts for back biasing the iron before each pulse. Requirements of ~ 920 (690) Wb for the 50%-50% (90%-10%) D-T fuel mixture cases results in 230 (170) m^2 of iron which represents about 3-4 times the amount of iron shown in Figs. 15 and 17. This additional amount of iron could be put around the torus, however diminishing space and added maintenance problems may be prohibitive. A second poloidal coil may be inserted outside the iron core to drive a fraction of the flux and reduce the iron requirements, although additional energy storage and ohmic losses are again incurred. This study has used the engineering Q-value Q_E as the object function for system optimization. The large amount of iron required represents an additional constraint which may alter the design point once an economic analysis is performed, which is beyond the scope of this work.

Conceptual designs of homopolar machines (16) for the Reference Theta Pinch Reactor provide the engineering basis for the RFPR energy storage system. Machines using low inertia rotors constructed of hollow, radially thin, cylinders allow increases in diameter, speed, and magnetic field with superconducting windings. These properties yield low energy storage costs and high efficiency.

The machine voltage is

$$V = v \bar{B}_R L \quad (5.7)$$

where the maximum allowable peripheral velocity v is taken as 277 m/s and the average field between collectors \bar{B}_R is 3 T. The voltage is then specified by the active length L of the machine. The energy stored in a cylindrical rotor machine is

$$W_S = \frac{\pi}{4} \rho L r_O^2 v^2 f_i \quad (5.8)$$

where the density ρ of the aluminum-graphite fiber rotor is 2300 kg/m³. Taking the fraction f_i of the flux intercepted by the rotor as 0.61 then defines the rotor radius r_O for the required machine energy W_S . This value of f_i is dependent upon a rotor length to diameter ratio of 0.75. This value is closely maintained in the design of the poloidal field system which is the major energy store. For the toroidal field system, length to diameter ratios of 0.5 - 0.75 are favorable. Size optimization leads to rotor diameters of 1.5 - 3 m with energy transfer efficiencies of ~95% and energy storage costs of ~0.6¢/Joule. These considerations lead to the homopolar parameters listed in Table 4.

The system requires the interruption of ~3 MA from two series connected homopolar generators. Using ~200 kA switches then requires a parallel set of 15 switches with the associated problem of current isolation during switching. The rapidly varying impedance of a switching element may result in one switch carrying all the current, unless precautions are taken. This may involve keeping the parallel circuits electrically separate (although inductive coupling will occur) and paralleled only at the brushes of the homopolar which also reduces circulating currents in the coils.

Table 4. Homopolar specifications

Energy Storage System	Risetime (s)	Voltage (kV)	Total Active Length (m)	Diameter (m)	Number of Rotors	Number of Machines	Energy Per Machine (MJ)
Poloidal (90%-10% DT)	0.1	4.5	5.42	2.35	4	20	635
Toroidal (90%-10% DT)	0.05	4.5	5.42	1.45	6	2	242
Poloidal (50%-50% DT)	0.1	5.5	6.62	2.27	4	30	720
Toroidal (50%-50% DT)	0.05	5.5	6.62	1.73	6	2	418

Solid state switching may be used for this system. The rating of these devices is about 200 kA at 4-6 kV and many of them are paralleled to give the desired current rating. The cost of this type of switching element is, however very high and probably prohibitive. The present price estimates (77) are $\$10^4/\text{MVA}$ with total requirements on the order of 5×10^4 MVA. This may be alleviated by using mechanical breakers or the A.E.G. air blast breaker to be used in JET (77). These breakers interrupt ~ 100 kA and cost $\sim \$0.5$ M which still results in a high cost considering 300-400 are needed. This problem may be alleviated by using hydraulic (oil) breakers (78) which can interrupt ~ 100 kA and may cost only $\sim \$2000$, although the reliability of these switches must be resolved.

VI. SUMMARY AND CONCLUSIONS

The physics model used herein predicts a wide range of possible operating points for the reversed-field pinch reactor. The operating range is, however, greatly reduced when considering first-wall thermal constraints and imposing an upper limit on the achievable current density. The ohmically ignited pulsed system must have a radius greater than about 1.5 m to minimize the recirculating power fraction which results in a reactor system of moderate power output (750 MWe). The reactor system that evolves from this model achieves an overall plant efficiency of 30-33% using a lithium-sodium-steam heat transport system which will use much of the technology developed from the Liquid-Metal Fast-Breeder Reactor. Preliminary consideration of major reactor subsystems reveals no major "flaws" although considerable technological development will be required before the reactor described herein could be fully realized.

Relatively slow startup is necessary to be compatible with the rotating machinery (homopolar generators) which provides the field energy. Establishing the RFP profiles may require the plasma to pass through many unstable states resulting in turbulence. For risetimes of 0.1 s the required voltages (5-6 kV) are achievable with homopolar generators. Electron runaway can be avoided during the early phases of breakdown and is not a problem when greater than 10% of the fuel is ionized. Laboratory experimentation must, however, reveal the true plasma behavior during long (~ 0.1 s) startup time periods.

The evaluation of various burn cycles must be based on the resultant recirculating power fraction and first-wall thermal constraints such as stress and thermal fatigue. Recirculating power fractions of ~ 0.25 are achievable in 50%-50% D-T systems in which the temperature rises uncontrollably until beta limits are achieved and the plasma must be quenched. Temperature control by heat loss from the plasma implies an enhanced surface heat flux at the first wall which imposes severe constraints in a pulsed high-density system. Using a 90%-10% D-T fuel mixture provides automatic temperature control by tritium burnup and results in recirculating power fractions of ~ 0.15 . The feasibility of these burn cycles must ultimately be investigated with a MHD burn code.

The operation of a RFPR in a pulsed mode is contingent upon extracting the plasma current at the end of the burn. This may require the reacting volume to be flooded with neutral gas during the quench phase in order to avoid a short-circuit current path at the first wall. The flux trapped in the wall-confined plasma at the end of the burn is assumed thermally lost to the wall. To replace this lost flux requires 50% of the recirculating electric power, which demonstrates the importance of the plasma quench and the need for detailed calculations to better quantify the actual amount of flux lost.

Stability of the plasma during the burn cycle is assumed. Constraints are imposed on the maximum poloidal beta, minimum plasma radius, and achievable current densities (experimentally determined); however, the conducting wall needed for complete stability would be too thick for a reactor system. The image currents necessary for stability

could be provided by the external coils for slowly growing modes (~ 0.01 s) in conjunction with a thin (1 cm) conducting wall to stabilize the rapidly growing modes. The need to prevent a slowly growing helical deformation is questionable. The large field trapped inside the plasma will prevent any large energy loss from the plasma even if in close proximity to the wall (as a tokamak). Much theoretical work is needed to determine the required thickness of the conducting wall.

The RFPR is a medium aspect ratio system which results in a low dipole field (1-2 T) in the center of the torus allowing the use of an unsaturated iron core to minimize the recirculating power fraction (maximize Q_E) although the large amount of iron required may ultimately change the design point due to restrictions on space and cost. The use of normal field coils requires only 10-20% of the recirculating electrical energy and greatly simplifies the construction and maintenance of the system when compared to superconducting coils.

Among the most difficult engineering problems of this system are the required high efficiency ($\sim 90\%$) energy transfer and storage. Homopolar generators provide a realistic solution to the energy storage problem; however, these devices require a significant technological development. The reliable switching of large amounts of energy (10-20 GJ) every ~ 10 s is perhaps the most formidable problem. Solid state switching is possible; however, the cost may prove to be prohibitive. The development of reliable mechanical switches at low cost may be necessary.

The study of a pulsed RFPR has revealed physics operating points that are compatible with realistic engineering systems. The desirability of these systems must await an economic assessment and is contingent upon favorable physics scaling.

VII. TOPICS FOR FURTHER STUDY

The reactor design generated by this thesis represents a basis from which a more comprehensive and realistic engineering system may be developed. The present design describes a plausible reactor scenario that is contingent on many physics and engineering assumptions that warrant further study.

Plasma behavior is subject to much conjecture due to the limited experimental work that has been performed on the RFP. Theoretical work dealing with startup, field reversal, stability/equilibrium and the associated need for a flux conserving first wall, transport loss, and a neutral-gas blanket (plasma quench) could provide insight into the behavior of a RFP plasma. The actual response of the plasma must be investigated through further experimentation, although "reactor-like" plasmas will not be available for many years.

A final design point will ultimately be dictated by economics which must be the underlying consideration in future parameter studies of the RFPR. This will also allow a refinement in the engineering design of major subsystems such as the first wall, blanket, toroidal/poloidal field coil, iron core, energy storage/transfer system, vacuum/fueling, and the balance of plant. This work should ultimately lead to a consistent engineering design of a RFPR that will operate at minimum cost.

VIII. LITERATURE CITED

1. Kruskal, M.D. 1954. Large-Scale Instability in the Stellarator. USAEC Rept. NYO-6045.
2. Shafranov, V.D. 1956. The Stability of a Cylindrical Gaseous Conductor in a Magnetic Field. *Atomnaya Energiya* (English Translation) 1:709-713.
3. Artsimovich, L.A. 1972. Tokamak Devices. *Nuclear Fusion* 12:215-252.
4. Dean, S.O., chairman. 1973. Status and Objectives of Tokamak Systems for Fusion Research. USAEC Rept. WASH-1295.
5. Toyama, H., et al. 1976. Experiments on Noncircular Tokamak and Related Topics. Sixth International Conference on Plasma Physics and Controlled Nuclear Fusion Research, Berchtesgaden, West Germany 6:IAEA-CN-35/A10-4.
6. Plasma Theory Section Staff. 1976. Tokamak Plasma Magnetics. Sixth International Conference on Plasma Physics and Controlled Nuclear Fusion Research, Berchtesgaden, West Germany 6:IAEA-CN-35/B10.
7. Chu, C.K., et al. 1975. Initial Dynamics, Equilibrium, and Heating of Toroidal Belt Pinches. Third Topical Conference on Pulsed High Beta Plasmas, Culham, United Kingdom 3:553-556.
8. Hoekzema, J.A. 1975. Toroidal Equilibrium of Non-Circular Sharp Boundary Plasmas Surrounded by Force-Free Fields. Third Topical Conference on Pulsed High Beta Plasmas, Culham, United Kingdom 3:535-539.
9. Hirano, Kei-ichi. 1975. Screw Pinches and High Beta Tokamak with Circular Cross-Section. Third Topical Conference on Pulsed High Beta Plasmas, Culham, United Kingdom 3:87-91.
10. Bobeldijk, C., et al. 1975. Results of SPICA. Third Topical Conference on Pulsed High Beta Plasmas, Culham, United Kingdom 3:493-496.
11. Bodin, H.A.B. 1975. Reversed Field Pinches. Third Topical Conference on Pulsed High Beta Plasmas, Culham, United Kingdom 3:39-57.
12. Baker, D. A., R. L. Hagenson, R. A. Krakowski, and K. I. Thomassen. 1977. Summary of the Reversed-Field Z-Pinch Concept. USERDA Rept. LA-UR-77-459. (Los Alamos Scientific Laboratory, Los Alamos, NM)

13. Baker, D.A. and J.N. DiMarco. 1975. The LASL Reversed-Field Pinch Program Plan. USERDA Rept. LA-6177-MS. (Los Alamos Scientific Laboratory, Los Alamos, NM)
14. Krakowski, R.A., R. L. Hagenson, and G.E. Cort. 1976. First Wall Wall Thermal-Mechanical Analyses of the Reference Theta-Pinch Reactor. Nuclear Technology 34(2):217-241.
15. Krakowski, R.A., et al. 1976. CTR-DOT Quarterly Report for the Period July 1 - September 30, 1976. (Los Alamos Scientific Laboratory, Los Alamos, NM)
16. Thomassen, K.I., et al. 1976. Conceptual Engineering Design of a One-GJ Fast Discharging Homopolar Machine for the Reference Theta-Pinch Fusion Reactor. EPRI ER-246, Project 469. (Electric Power Research Institute)
17. Glasstone, S. and R.H. Lovberg. 1960. Controlled Thermonuclear Reactions. Van Nostrand Reinhold Company, New York, N.Y. 523 pp.
18. Rose, D.J. and M. Clark, Jr. 1965. Plasmas and Controlled Fusion. 2nd ed. The M.I.T. Press, Massachusetts Institute of Technology, Cambridge, Massachusetts. 493 pp.
19. Kruskal, M.D. and M. Schwarzschild. 1954. Some Instabilities of a Completely Ionized Plasma. Proceedings of the Royal Society of London A223:348-360.
20. Tayler, R.J. 1957. Hydromagnetic Instabilities of an Ideally Conducting Fluid. Physical Society B70:31-48.
21. Rosenbluth, M.N. 1956. Stability of the Pinch. USAEC Rept. LA-2030. (Los Alamos Scientific Laboratory, Los Alamos, NM)
22. Shafranov, V.D. 1957. On the Stability of a Cylindrical Gaseous Conductor in a Magnetic Field. J. Nuclear Energy 5:86-91.
23. Tayler, R.J. 1958. The Stability of a Constricted Gas Discharge. Proceedings of the Second United Nations International Conference on the Peaceful Uses Atomic Energy, Geneva, Switzerland 2(31):160-170.
24. Kruskal, M. and J. L. Tuck. 1958. The Instability of a Pinched Fluid with a Longitudinal Magnetic Field. Proceedings of the Royal Society of London A245:222-237.
25. Suydam, R.B. 1958. Stability of a Linear Pinch. Proceedings of the Second United Nations International Conference on the Peaceful Uses of Atomic Energy, Geneva, Switzerland 2(31):157-159.

26. Newcomb, W.A. 1960. Hydromagnetic Stability of a Diffuse Linear Pinch. *Annals of Physics* 10:232-267.
27. Furth, H.P. 1960. Sufficient Conditions for Hydromagnetic Stability of a Diffuse Linear Pinch. *Physics of Fluids* 3:977-981.
28. Suydam, B.R. 1960. Stability of a Linear Pinch, Part II. USAEC Rept. LAMS-2381. (Los Alamos Scientific Laboratory, Los Alamos, NM)
29. Baker, D.A. and L.W. Mann. 1974. Progress Report of the LASL Controlled Thermonuclear Research Program. USERDA Rept. LA-5656-PR. (Los Alamos Scientific Laboratory, Los Alamos, NM)
30. Baker, D.A., et al. 1971. Z-Pinch Experiments with Shock Heating. Proceedings of the IAEA Conference on Plasma Physics and Controlled Nuclear Fusion Research, Madison, Wisconsin 4(1):203-216.
31. Robinson, D.C. 1971. High- β Diffuse Pinch Configurations. *Plasma Physics* 13:439-462.
32. Mercier, C. 1960. A Necessary Criteria of Hydromagnetic Stability for a Plasma with Symmetry of Revolution. *Nuclear Fusion* 1:47-53.
33. Baker, D.A. and L.W. Mann. 1972. MHD Studies of Numerically Obtained Toroidal Equilibria. Proceedings of the Second Topical Conference on Pulsed High Beta Plasmas, Munich, West Germany 2:69-72.
34. Haberstich, D.A., et al. 1975. Stability and Diffusion of the ZT-I Reversed Field Pinch. Third Topical Conference on Pulsed High Beta Plasmas, Culham, England 3:249-253.
35. Crow, J.E., J. Kileen, and D.C. Robinson. 1973. Resistive Instabilities in Diffuse Pinches. Proceedings of the Sixth European Conference on Controlled Fusion and Plasma Physics, Moscow USSR 6(1):269-272.
36. Diabise, J.A. 1974. Numerical Studies of Resistive Instabilities in Diffuse Pinches. USERDA Rept. UCRL-51591. (Lawrence Livermore Laboratory, Livermore, CA)
37. Butt, E.P., et al. 1974. Confinement and Stability of High Beta Plasma in a Reversed Field Pinch. Proceedings of the Fifth International Conference on Plasma Physics and Controlled Nuclear Fusion Research, Tokyo, Japan 5(3):417-429.

38. Turner, L. 1977. Vlasov-Fluid Theory of Short Wavelength Instabilities of a Sharp-Boundary Screw Pinch. *Phys. Fluids* 20(4):662-674.
39. Taylor, J.B. 1974. Relaxation of Toroidal Plasma and Generation of Reverse Magnetic Fields. *Phys. Rev. Letts.* 33(19): 1139-1141.
40. Ortolani, S. and G. Rostagni. 1975. Reverse Field Configurations with Minimum Potential Energy. Third Topical Conference on Pulsed High Beta Plasmas, Culham, UK 3:335-339.
41. Baker, D.A. and J.A. Phillips. 1974. Pressure-Balance Limitations in Z-Pinches with Diffusion Heating. *Phys. Rev. Letts.* 32(5):202-205.
42. Sgro, A.G. and C.W. Nielson. 1975. Hybrid Model Studies of Magnetic Field Diffusion in High- β Pinches. Third Topical Conference on Pulsed High Beta Plasmas, Culham, UK 3:329-334.
43. Burkhardt, L.C. 1975. Partial Chronology of Z-Pinch Studies at Los Alamos Scientific Laboratory, 1952-1975. USERDA Rept. LA-5922-H. (Los Alamos Scientific Laboratory, Los Alamos, NM)
44. Ohkawa, T., H.K. Forsen, A.A. Schupp, Jr., and D.W. Kerst. 1963. Toroidal Discharge Experiments with Rapid Programming. *Phys. Fluids* 6(6):846-857.
45. Butt, E.P., et al. 1958. The Design and Performance of ZETA. Proceedings of the Second United Nations International Conference on the Peaceful Uses of Atomic Energy, Geneva, Switzerland 32:42-64.
46. Burton, W.M., et al. 1962. Plasma Loss in ZETA. *Nuclear Fusion, Supplement* 3:903-919.
47. Butt, E.P., et al. 1965. Conditions for Improved Stability in ZETA. Proceedings of the Conference on Plasma Physics and Controlled Nuclear Fusion Research, Culham, UK 1:751-764.
48. Robinson, D.C. and R.E. King. 1968. Factors Influencing the Improved Stability of ZETA. Proceedings of the Third International Conference on Plasma Physics and Controlled Nuclear Fusion Research, Novosibirsk, USSR 3(1):263-276.
49. Butt, E.P. and A.A. Newton. 1975. New Results from ZETA. Third Topical Conference on Pulsed High-Beta Plasmas, Culham, UK 3:425-429.

50. Verhage, A.J.L. and D.C. Robinson. 1975. Stability of Pinches with a Reversed Field in HBTX I. Third Topical Conference on Pulsed High Beta Plasmas, Culham, UK 267-271.
51. Bunting, C.A., A.A. Newton, and M.R.C. Watts. 1975. Studies of the Ion Temperature and Total Radiated Energy from Pinches in HBTXI. Third Topical Conference on Pulsed High Beta Plasmas, Culham, UK 3:437-441.
52. Buffa, A., S. Costa, G.F. Nalesso, and G. Malesani. 1975. Experiments on Programmed and Naturally Relaxing RFP Configurations. Third Topical Conference on Pulsed High Beta Plasmas, Culham, UK 3:261-265.
53. Buffa, A., et al. 1976. Heating, Diffusion, and Stability of Reverse Field Pinch Configurations. Sixth International Conference on Plasma Physics and Controlled Nuclear Fusion Research, Berchtesgaden, West Germany 6:IAEA-CN-35/E3.
54. Ogawa, K., et al. 1975. High Beta Plasma Confinement in Reversed Field Pinch (ETL TPE-1). Third Topical Conference on Pulsed High Beta Plasmas, Culham, UK 3:255-259.
55. Shimada, T., et al. 1976. Toroidal Pinch Experiments in ETL. Sixth International Conference on Plasma Physics and Controlled Nuclear Fusion Research, Berchtesgaden, West Germany 6:IAEA-CN-35/E4.
56. Hirano, K., et al. 1976. Plasma Confinement of Nagoya High Beta Toroidal Pinch Experiments. Sixth International Conference on Plasma Physics and Controlled Nuclear Fusion Research Berchtesgaden, West Germany 6:IAEA-CN-35/E7.
57. Baker, D.A., et al. 1971. Z-Pinch Experiments with Shock Heating. Proceedings of the IAEA Conference on Plasma Physics and Controlled Nuclear Fusion Research, Madison, Wisconsin 1:203-216.
58. Burkhardt, L.C., et al. 1972. Recent Results from the Shock Heated Toroidal Z-Pinch Experiment ZT-I. Proceedings of the Second Topical Conference on Pulsed High Beta Plasmas, Munich, West Germany 2:33-36.
59. Bodin, H.A.B., T.E. James, and A.A. Newton. 1969. A Pulsed Fusion Reactor Based on the Toroidal Pinch. Proceedings of the BNES Nuclear Fusion Reactor Conference, Culham, UK 1:3.4.
60. Bodin, H.A.B., et al. 1975. The Pulsed Reverse Field Pinch Reactor. Plasma Physics and Controlled Nuclear Fusion Research, Vienna, Austria 1:IAEA-CN-33/G5.

61. Yeung, B.C., J.W. Long and A.A. Newton. 1975. Reactor Burning Calculations for a Model Reversed Field Pinch. Third Topical Conference on Pulsed High Beta Plasmas, Culham, UK 3:575-579.
62. Hancox, R., et al. 1977. A 600 MW(e) Reversed Field Pinch Reactor Study. IAEA Workshop on Fusion Reactor Design, Madison, Wisconsin, 1:CLM-P501.
63. Newton, A.A., Li Yin-An, J.W. Long, and B.C. Yeung. 1975. Numerical Investigation of Reversed Field Pinches. Third Topical Conference on Pulsed High Beta Plasmas., Culham, UK 3:323-328
64. Thomassen, K. I., et al. 1977. Ohmic Heating Systems Study for a Tokamak EPR. USERDA Rept. LA-UR-77-398. (Los Alamos Scientific Laboratory, Los Alamos, NM)
65. Krajcik, R.A. 1973. The Effect of a Metallic Reflector upon Cyclotron Radiation. Nuclear Fusion 13:7.
66. Burnett, S.C., W.R. Ellis, T. A. Oliphant, and F. L. Ribe. 1972. A Reference Theta Pinch Reactor (RTPR). USAEC Rept. LA-5121-MS. (Los Alamos Scientific Laboratory, Los Alamos, NM)
67. Oliphant, T.A. 1969. Fuel Burnup and Direct Conversion of Energy in a D-T Plasma. USAEC Rept. LA-DC 10528. (Los Alamos Scientific Laboratory, Los Alamos, NM)
68. Papoular, R. 1976. The Genesis of Toroidal Discharges. Nuclear Fusion 16:37-45.
69. Bernstein, W., F.F. Chen, M.A. Heald, and A.Z. Kranz. 1958. "Run-away" Electrons and Cooperative Phenomena in B-1 Stellarator Discharges. Physics of Fluids 1(5):430-437.
70. Coor, T., et al. 1958. Experiments on the Ohmic Heating and Confinement of Plasma in a Stellarator. Physics of Fluids 1(5):411-420.
71. Berger, J.M., I.B. Bernstein, E.A. Frieman, and R.M. Kulsrud. 1958. On the Ionization and Ohmic Heating of a Helium Plasma. Physics of Fluids 1(4):297-300.
72. Gurevich, A.V. 1961. On the Theory of Runaway Electrons. Soviet Physics JETP 12(5):904-912.
73. Krakowski, R.A., F.L. Ribe, T.A. Coultas and A.J. Hatch. 1974. An Engineering Design of a Reference Theta-Pinch Reactor (RTPR). USAEC Rept. LA-5336/ANL-8019.

74. Dushman, S. and J.M. Lafferty. 1965. Scientific Foundations of Vacuum Technique. John Wiley and Sons, Inc., New York, NY. 806 pp.
75. Cort, G.E. and R. A. Krakowski. 1978. Heat Transfer in Lithium-Cooled Blanket of the Reference Theta-Pinch Reactor. To be presented at the Sixth International Heat Transfer Conference, Toronto, Canada.
76. Armstrong, P.E. and R.A. Krakowski. 1977. Thermal Shock Experiment (TSEX): A "Proof-of-Principle" Evaluation of the Use of Electron Beam Heating to Simulate the Thermal Mechanical Environment Anticipated for the First Wall of the Reference Theta-Pinch Reactor (RTPR). USERDA Rept. LA-6861-MS. (Los Alamos Scientific Laboratory, Los Alamos, NM)
77. Heck, F.M., E.I. King, Jr., and R.E. Stillwagon. 1976. Experimental Power Reactor Ohmic Heating Energy Storage Study. WFPS-TME-038 (Westinghouse Electric Corporation, Fusion Power Systems Department).
78. Vogel, H.F. 1977. personal communication, Los Alamos Scientific Laboratory, Los Alamos, NM.
79. Spitzer, L. 1962. Physics of Fully Ionized Gases. Interscience Publishers, Inc., New York, NY. 105 pp.
80. Braginskii, S.I. 1965. Reviews of Plasma Physics Vol. 1. Consultants Bureau, New York, NY. 326 pp.

IX. ACKNOWLEDGMENTS

The performance of this research at the Los Alamos Scientific Laboratory has proved to be a very rewarding experience. I am especially grateful to Drs. Keith Thomassen, Robert Krakowski, and Zeinab Sabri for making this research arrangement possible, providing encouragement and support while supervising this research, and reviewing this manuscript. I also wish to acknowledge my appreciation to the many people who gave assistance and advice, including Celina Ortiz for her help in preparing this manuscript.

Special thanks go to my wife, Mary Jane, and daughter, Leigh, for their patience and support during my graduate studies. Their help has been invaluable.

The author was enrolled in the Nuclear Engineering Department at Iowa State University while performing this work. A fellowship provided by Associated Western Universities supported this research at the Los Alamos Scientific Laboratory under the auspices of the U.S. Energy Research and Development Administration.

X. APPENDIX

The classical plasma resistivities used in this study are given by Spitzer (79) as

$$\eta_{\parallel} = \frac{9.62 \times 10^{-10} Z_{\text{eff}} \ln \Lambda}{\gamma_E T_e^{3/2}} \quad (\Omega\text{-m}) \quad (\text{A.1})$$

$$\eta_{\perp} = \eta_{\parallel} / 0.51 \quad (\text{A.2})$$

where the value of γ_E is approximately

$$\gamma_E \approx 0.582 + 0.418 \left(\frac{Z_{\text{eff}}^{-1}}{Z_{\text{eff}}} \right)^2 \quad (\text{A.3})$$

and

$$\Lambda = \frac{4.907 \times 10^{17}}{Z_{\text{eff}}} \frac{T_e^{3/2}}{n_e^{1/2}} \quad , \quad T_e < 0.0362 \text{ keV} \quad (\text{A.4})$$

$$\Lambda = \Lambda \left(\frac{0.0362}{T_e} \right)^{1/2} \quad , \quad T > 0.0362 \text{ keV} \quad . \quad (\text{A.5})$$

The classical thermal conductivity perpendicular to field lines is given by Braginskii (80) as

$$k_{\perp} = 5.07 \times 10^{-39} \frac{a_i^{1/2} r_i^2 \ln \Lambda}{T_i^{1/2} B^2} \quad (\text{W/m keV}) \quad (\text{A.6})$$

where a_i is the atomic mass of the ions ($a_i = 2.5$ for DT fuel) and B is somewhat arbitrarily taken as B_0 at the radius r_p .